Second-generation stoichiometric mathematical model to predict methane emissions from oil sands tailings

Jude D. Kong[1,2], Hao Wang[2*†], Tariq Siddique[3*‡], Julia Foght[4], Kathleen Semple[4], Zvonko Burkus[5], and Mark A. Lewis[2,4]

[1]Center for Discrete Mathematics and Theoretical computer Science, Rutgers University, 96 Frelinghuysen Road Piscataway, NJ 08854-8018, USA

[2]Department of Mathematical and Statistical Sciences, University of Alberta, Edmonton, AB T6G 2G1, Canada

[3]Department of Renewable Resources, University of Alberta, Edmonton, AB T6G 2G7, Canada

[4]Department of Biological Sciences, University of Alberta, Edmonton, AB T6G 2E9, Canada

[5]Alberta Environment and Parks, Government of Alberta, Edmonton, Canada

Corresponding authors' emails:

[*†] Mathematical approach (Hao Wang); hao8@ualberta.ca

[*‡] Biological approach (Tariq Siddique); tariq.siddique@ualberta.ca

Abstract

Microbial metabolism of fugitive hydrocarbons produces greenhouse gas (GHG) emissions from oil sands tailings ponds (OSTP) and end pit lakes (EPL) that retain fluid tailings from surface mining of oil sands ores. Predicting GHG production, particularly methane (CH_4), would help oil sands operators mitigate tailings emissions and may assist regulators evaluating the trajectory of reclamation scenarios. Using empirical datasets from laboratory incubation of OSTP sediments with pertinent hydrocarbons, we developed a stoichiometric model for CH_4 generation by

indigenous microbes. This model improved on previous first-approximation models by considering long-term biodegradation kinetics for 18 relevant hydrocarbons from three different oil sands operations, lag times, nutrient limitations, and microbial growth and death rates. Laboratory measurements were used to estimate model parameter values and to validate the new model. Goodness of fit analysis showed that the stoichiometric model predicted CH_4 production well; normalized mean square error analysis revealed that it surpassed previous models. Comparison of model predictions with field measurements of CH_4 emissions further validated the new model. Importantly, the model also identified parameters that are currently lacking but are needed to enable future robust modeling of CH_4 production from OSTP and EPL in-situ.

Keywords: modeling methane production; anaerobic hydrocarbon biodegradation; methanogenesis; greenhouse gas emissions; oil sands tailings pond; end pit lake

1. Introduction

Alberta's oil sands industry is a major economic driver in Canada, currently producing ~3 million barrels oil d^{-1} and expected to reach 4 million barrels d^{-1} by 2024 (Government of Alberta, 2019a; https://aer.ca/providing-information/data-and-reports/statistical-reports/st53). However, the oil sands sector has come under international scrutiny regarding GHG emissions and other environmental issues. Oil sands operations including mining, upgrading and in-situ extraction were responsible for ~43% of Alberta's overall GHG emissions in 2012 (Alberta Greenhouse Gas Report, 2016). In addition to these production operations, the storage and management of aqueous slurries of surface-mined ore processing wastes in oil sands tailings ponds (OSTP; Figure S1) contributes substantially to methane (CH_4) and carbon dioxide (CO_2) emissions (Burkus et al., 2014; Siddique et al., 2008). Total fugitive GHG emissions from major oil sands operators' OSTP, measured in-situ using floating flux chambers in 2011, were calculated to be 2.8 million tonnes CO_2 equivalent per year (Burkus et al., 2014), while in 2018 they were estimated at ~2.2 Mt of CO_2e (Z. Burkus, personal communication). Furthermore, proposed implementation of EPL as a long-term reclamation strategy for OSTP sediments (Figure S1) may contribute additional GHG emissions for an unknown timespan.

During five decades of retention, enormous volumes of tailings have accumulated that is currently estimated at >1.2 billion m^3 (Government of Alberta, 2019b). As the fluid tailings in OSTP age, the suspended clay fines settle via several mechanisms (porewater and solid phase chemistry) including gravity (Siddique et al., 2014) to become anaerobic mature fine tailings (MFT) having a solids content >30 wt% and possessing both an active microbiota and residual diluent in progressive stages of selective biodegradation (Fig S2 in Foght et al., 2017). The use of EPL has been discussed to reintegrate the accumulated tailings into the on-site environment (Charette et al., 2012) and proposed by industry in their tailings management plans as one of their closure approaches (Alberta Energy Regulator, 2019). In this reclamation scenario, after

years or decades of residence in OSTP, MFT would be treated and transported to mined-out pits and capped with fresh water and/or process-affected water. This is intended to establish a sustainable aquatic system (i.e., an end pit lake; EPL) that, with time, should support economic, ecological and/or societal uses (Charette et al., 2012). However, ebullition of GHG from underlying sediments may delay EPL ecosystem development by dispersing fine sediments into the overlying water layer along, potentially co-transporting some constituents of concern. Thus, GHG emissions from oil sands tailings repositories are problematic from global warming as well as ecological standpoints.

GHG emissions from OSTP and EPL result primarily from anaerobic biodegradation of diluent hydrocarbons, naphtha or light paraffins, introduced into tailings after aqueous extraction of bitumen from oil sands ore and treatment of froth (Figure S1; reviewed in Foght et al., 2017) The diluents, specific to each operator, facilitate separation of bitumen from water and mineral solid particles during froth treatment and reduce bitumen viscosity in preparation for processing and/or transport. Most of the diluent is recovered from the froth treatment tailings for re-use, but a small proportion remains in the tailings slurry that comprises alkaline water, sand, silt, clays and unrecovered bitumen. These fresh tailings, as well as other tailings streams that have not been exposed to diluent, are deposited in OSTP where indigenous anaerobic microbial communities biodegrade the labile hydrocarbons to CH_4 and CO_2 (Abu Laban et al., 2015; Penner and Foght, 2010; Mohamad Shahimin et al., 2016; Siddique et al., 2011). Although naphtha and paraffinic diluents are considered to be the major carbon sources for microbes in OSTP (Foght et al., 2017), only certain of their hydrocarbon components are known to be biodegradable under anaerobic conditions, whereas others are recalcitrant (slowly or incompletely biodegraded) or are completely resistant to biodegradation (Siddique et al., 2018).

Although bitumen is the overwhelming organic constituent of fresh tailings, it predominantly comprises recalcitrant hydrocarbons: only a small proportion may be labile and the contribution of bitumen to biogenic GHG is thought to be negligible in proportion to that of diluent (Foght et al., 2017).

The importance of modeling GHG emissions is clear to oil sands operators, as it provides a rationale for mitigating GHG mitigation efforts and managing OSTP and EPL. However, field data (e.g., concentrations of individual hydrocarbons in OSTP, nutrient concentrations, biomass) needed for modeling are generally unavailable either because collection of such data is technologically difficult or because such key model parameters have not previously been identified as necessary. Therefore, we have cultivated MFT in laboratory cultures analogous to OSTP and EPL for use in initial modeling efforts. A previous study (Siddique et al., 2008) used limited data available from short-term (<1 yr) laboratory studies measuring biodegradation of a small subset of components (Siddique et al., 2007, 2006) in a single naphtha diluent to develop zero- and first-order kinetic models for estimating CH_4 production potential from a single OSTP. That first approximation model predicted in-situ CH_4 production volumes reasonably consistent with emissions measured in-situ (Siddique et al., 2008). However, in the decade since that work, additional components of naphtha and paraffinic diluent have been shown to support methanogenesis from MFT during extended laboratory incubation (up to 6.5 y; Abu Laban et al., 2015; Mohamad Shahimin et al., 2016; Siddique et al., 2015, 2011). This finding increases theoretical GHG emissions, especially from hydrocarbons previously assumed to be recalcitrant and thus not considered in the previous model and over extended time scales more relevant to long-term retention of tailings. Additionally, data are now available for additional OSTP receiving different diluents and therefore having unique microbial communities (Wilson et al.,

2016) with different CH_4 production potentials, and the effect of potentially growth-limiting nutrients in-situ such as nitrogen has begun to be examined (Collins et al., 2016). Also, the first EPL field trial was established in 2012/2013 where CH_4 has been detected within the water cap (Risacher et al., 2018). The greatly expanded data set and a broader understanding of oil sands tailings microbiology (Foght et al., 2017) enable and have driven development of the improved and flexible model for CH_4 generation described here.

The goals of the new stoichiometric model were: (1) to expand CH_4 predictive capability by considering methanogenic biodegradation of a wider range of hydrocarbons only recently shown to be labile over longer incubation times; (2) for the first time to consider OSTP that receive diluents having different compositions and that harbour different microbial communities; (3) to account for the effects of nutrient limitation on CH_4 generation, particularly available nitrogen; (4) to compare model predictions with field measurements of CH_4 emissions to validate the model and reveal any shortcomings; (5) to consider differences in GHG emission trajectories between OSTP and EPL; and (6) to identify parameters essential for future development of a model to predict CH_4 emissions in-situ in OSTP and EPL.

2. Materials and Methods

Although the gaseous products of methanogenic hydrocarbon biodegradation are CH_4 and CO_2 (Figure S2), the stoichiometric model developed here considers only CH_4 production for two reasons: CH_4 has a greater greenhouse effect than CO_2; and measurement of emissions of CO_2 emissions produced in MFT is confounded by abiotic (carbonate dissolution) and biogeochemical (mineral precipitation and dissolution) interactions with tailings minerals (Siddique et al., 2014), complicating measurement and modeling.

Methane production from hydrocarbons involves two microbial processes: the oxidation of labile hydrocarbons to simple organic compounds by Bacteria and the conversion of those compounds to CH_4 and CO_2 by Archaea (Figure S2). Therefore, the model was developed in two modules. The first module (section 2.1) comprising two systems of equations describes bacterial biodegradation of 18 hydrocarbon substrates (see section 2.3.1 for selection rationale) and includes formation of microbial biomass. The second module (section 2.2) considers archaeal CH_4 generation from bacterial metabolites. Model parameters unavailable in the literature were estimated by data fitting using laboratory measurements (section 2.3). The model then was quantitatively validated by comparison (1) to measurements from independent but analogous laboratory experiments conducted using oil sands tailings incubated with whole diluents or components of naphtha or paraffinic diluents and (2) to field measurements of CH_4 emissions from OSTP (section 2.4). Finally the model was qualitatively assessed using phase plane analysis to illustrate CH_4 emission trajectories in OSTP and EPL (section 2.5 and supporting material section S3). Terms used in model development are defined in Table 1.

2.1 Biodegradation and biomass module development.

Direct measurement of hydrocarbon biodegradation kinetics in OSTP and EPL is technically infeasible. Therefore this module describes the dynamics of CH_4 production from MFT incubated with cognate naphtha or paraffinic diluents under laboratory conditions analogous to those expected in OSTP or EPL. A brief description of previously published cultivation methods used to generate model data is given in supporting material section S1.

Microbial biomass can change as a result of growth and death. Because hydrocarbon biodegradation is initiated by Bacteria and not by the archaeal methanogens (Figure S2), this module considers only bacterial kinetics. The per cell bacterial growth rate is assumed to follow

Liebig's law of the minimum (Sterner and Elser, 2002) stating that growth rate is proportional to the most limiting resource available. The model assumes, based on chemical analysis of oil sands tailings (Collins, 2013; Penner and Foght, 2010) that all relevant nutrients except biologically-available nitrogen (defined in Table 1) and/or labile carbon are present at non-limiting concentrations in OSTP and EPL. Therefore the bacterial growth rate is modeled as a function only of the mass of biologically-available nitrogen (N_A) and labile hydrocarbons (C_i, the mass of labile hydrocarbons in the system for i=1…n, assuming n discrete labile hydrocarbons in the system). Assuming that there is negligible input of N_A with fresh tailings, no outflow of soluble N_A and no loss of gaseous NO_x, we take the total nitrogen (N_T) in these systems to be constant. With this assumption, the subset of N_T available for bacterial growth (N_A) is given by $N_A = N_T - \theta B$ where θ is the ratio of nitrogen to carbon in the total microbial biomass B, and θ is assumed to be constant (Makino et al., 2003). The Monod functions $f(N_A) = \frac{N_A}{N_A + K_f}$ and $g(C_i) = \frac{C_i}{C_i + K_{g_i}}$ are used to model the nitrogen- and carbon-dependent growth rates respectively, where K_f is the N_A-dependent half-saturation constant; K_{g_i} is the C_i-dependent half-saturation constant; and C_i^{in} is the inflow of C_i to the system. Thus, the C_i-dependent per cell bacterial growth rate μ is given by $\mu_i \min\{f(N_A), g(C_i)\}$, where μ_i is the maximum growth rate of bacteria growing on only the hydrocarbon C_i present and is unique for each labile hydrocarbon. Hence the total per cell growth rate of bacteria is $\sum_{i=1}^{n} \mu_i \min\{f(N_A), g(C_i)\}$.

The biodegradation rate of each labile hydrocarbon i is assumed to be proportional to the bacterial growth rate due to its consumption, i.e., [per cell bacterial growth rate due to each hydrocarbon] ∝ [biodegradation rate of hydrocarbon]. This implies that [the per cell bacterial growth rate supported by each labile hydrocarbon i)] = r_i[the per cell biodegradation rate of that hydrocarbon] where r_i is a proportionality constant reflecting the efficiency of bacterial

conversion of substrate into biomass. Hence, [the per cell biodegradation rate of each labile hydrocarbon] = $\frac{1}{r_i}$ [the per cell bacterial growth rate supported by labile hydrocarbons], i.e., [the per cell biodegradation rate of each hydrocarbon] = $\sum_{i=1}^{n}\frac{1}{r_i}\mu_i \min\{f(N_A), g(C_i)\}$. Archaeal growth and death are considered in the second module (section 2.2).

We assume that microbial death rate (d) is constant in the laboratory cultures and that nutrients in dead microbial biomass are quickly recycled back into labile carbon and nitrogen (N_A). The fraction of C_i recycled from dead biomass b is assumed to be a constant β_i where $0 < \beta_i < 1$.

In accordance with laboratory observations (Mohamad Shahimin and Siddique, 2017a, 2017b, Siddique et al., 2007, 2006), the model assumes that onset of biodegradation of each hydrocarbon begins after a unique lag period, λ_i. The above assumptions lead to the following system of equations:

$$g(C_i) = \begin{cases} 0, & t < \lambda_i \\ \dfrac{C_i}{K_{g_i} + C_i}, & t \geq \lambda_i \end{cases}$$

$$\frac{dB}{dt} = B\sum_{i=1}^{n}\mu_i min\left\{\frac{N_A}{K_f + N_A}, g(C_i)\right\} - dB, \qquad (1)$$

$$\frac{dC_i}{dt} = \frac{-1}{r_i}\mu_i B min\left\{\frac{N_A}{K_f + N_A}, g(C_i)\right\} + \beta_i dB + C_i^{in},$$

$$N_A = N_T - \theta B,$$

$$B(0) > 0, C_i(0) \geq 0.$$

Since the carbon- and nutrient-dependent growth efficiency parameters describe the main differences in bacterial utilization of different hydrocarbon, the model assumes that parameters such as carbon conversion efficiency, intrinsic bacterial growth rate, and carbon recycling from

dead bacteria (negligible in our data fitting), are equivalent for different hydrocarbons; i.e., $\mu_i = \mu, r_i = r$, and $\beta_i = \beta$. With this assumption, the system of equations becomes:

$$g(C_i) = \begin{cases} 0, & t < \lambda_i \\ \dfrac{C_i}{K_{g_i} + C_i}, & t \geq \lambda_i \end{cases}$$

$$\frac{dB}{dt} = B \sum_{i=1}^{n} \mu min\left\{\frac{N_A}{K_f + N_A}, g(C_i)\right\} - dB, \qquad (2)$$

$$\frac{dC_i}{dt} = \frac{-1}{r} \mu B min\left\{\frac{N_A}{K_f + N_A}, g(C_i)\right\} + \beta dB + C_i^{in},$$

$$N_A = N_T - \theta B,$$

$$B(0) > 0, C_i(0) \geq 0.$$

To analyze the types of solutions that this model could produce, a steady state analysis was performed. The algebraic analysis is described in supplementary material section S2 and is of particular use because it allows solutions to be classified by parameter values.

2.2 Methane biogenesis module development

From the preceding biodegradation module, bacterial biodegradation of a hydrocarbon substrate (C_i) per unit time yields $\frac{1}{r} \mu B min\left\{\frac{N_A}{K_f + N_A}, g(C_i)\right\}$ units of metabolite(s) corresponding to C_i. The metabolite(s) ultimately are converted to CH_4 and CO_2 (G_i) by methanogens (Figure S2). Since methanogens have a slow growth rate compared to that of the hydrocarbon-degrading Bacteria (being dependent on their metabolism), we assume that the biomass of methanogens in the system is constant. With these additions, the system of equations (2) becomes:

$$(C_i) = \begin{cases} 0, & t < \lambda_i \\ \dfrac{C_i}{K_{g_i} + C_i}, & t \geq \lambda_i \end{cases}$$

$$\frac{dB}{dt} = B \sum_{i=1}^{n} \mu min\left\{\frac{N_A}{K_f + N_A}, g(C_i)\right\} - dB\,, \tag{3}$$

$$\frac{dC_i}{dt} = \frac{-1}{r}\mu B min\left\{\frac{N_A}{K_f + N_A}, g(C_i)\right\} + \beta dB + C_i^{in}\,,$$

$$\frac{dG_i}{dt} = \frac{1}{r}\mu B min\left\{\frac{N_A}{K_f + N_A}, g(C_i)\right\},$$

$$\mathrm{CH_4} = \sum_{i=1}^{n} \eta_i \Gamma_i G_i,$$

$$N_A = N_T - \theta B,$$

$$B(0) > 0, C_i \geq 0, G_i(0) = 0$$

where, Γ_i is the maximum theoretical yield of CH_4 expected from biodegradation of one mole of C_i. This value can be calculated from Equation (4) (derived from Symons and Buswell, 1933, as implemented by Roberts, 2002) that describes the complete oxidation of hydrocarbons to CH_4 and CO_2 under methanogenic conditions, namely:

$$C_c H_h + \left(c - \frac{h}{4}\right) H_2 O \rightarrow \left(\frac{c}{2} - \frac{h}{4}\right) CO_2 + \left(\frac{c}{2} + \frac{h}{8}\right) CH_4 \tag{4}$$

where c and h are, respectively, the numbers of carbon and hydrogen atoms in a C_i molecule.

From equation (4), $\Gamma_i = \left(\frac{c}{2} + \frac{h}{8}\right)$. Furthermore, η_i is the fraction of the theoretical CH_4 yield from the biodegradation of a mole of C_i (i.e., a conversion efficiency factor) and is assumed to be the same for all C_i, i.e., $\eta_i = \eta$, with $0<\eta_i<1$. The values of $\eta_i$used in numerical simulations were obtained from (Mohamad Shahimin et al., 2016; Mohamad Shahimin and Siddique, 2017a, 2017b, Siddique et al., 2007, 2006) and Table S1.

2.3 Acquisition of laboratory data, parameter estimation and model validation

Our approach was to select a suite of 18 relevant labile hydrocarbons to generate model predictions, then estimate missing model parameters using empirical biodegradation kinetics and CH_4 measurements for these hydrocarbons, and finally to test the stoichiometric model quantitatively using measurements from an independent set of laboratory experiments.

2.3.1 Model hydrocarbon selection and testing

Fugitive diluent in froth treatment tailings (Fig. S1) is the predominant substrate for methanogenesis in OSTP (Foght et al., 2017). The most commonly used diluents are naphtha and paraffinic solvent. Syncrude Canada Ltd. (Syncrude), Suncor, and Canadian Natural Resources Ltd. (CNRL) use naphtha, the composition of which differs slightly for each company but which comprises primarily paraffinic (*n*-, *iso*- and *cyclo*-alkanes) and monoaromatic hydrocarbons (predominantly toluene and three xylene isomers), typically in the C_6-C_{10} range (Siddique et al., 2008). Canadian Natural Upgrading Limited (CNUL; formerly Shell Albian), Imperial (Kearl Mine) and Suncor (Fort Hills Mine) uses a paraffinic diluent comprising *n*- and *iso*-alkanes primarily in the C_5-C_6 range (Mohamad Shahimin and Siddique, 2017a). Published results from laboratory experiments incubating these whole diluents or their major constituents with MFT from Syncrude, CNUL or CNRL (Mohamad Shahimin et al., 2016; Mohamad Shahimin and Siddique, 2017a, 2017b, Siddique et al., 2007, 2006; and Table S1) revealed complete or significant biodegradation of 18 hydrocarbons under methanogenic conditions, including the *n*-alkanes *n*-pentane (C_5), *n*-hexane (C_6), *n*-heptane (C_7), *n*-octane (C_8), *n*-nonane (C_9), and *n*-decane (C_{10}); the *iso*-alkanes 2-methylpentane (2-MC_5), 2-methylhexane (2-MC_6), 3-methylhexane (3-MC_6), 2-methylheptane (2-MC_7), 4-methylheptane (4-MC_7), 2-methyloctane

253 (2-MC_8), 3-methyloctane (3-MC_8) and 2-methylnonane (2-MC_9); and the monoaromatics
254 toluene, *o*-xylene and *m*- plus *p*-xylenes (the latter two are not resolved by our gas
255 chromatography column and are therefore reported as a sum). Table 2 lists the 18 labile
256 hydrocarbons selected for model development, the source of biodegradation data, the type of
257 tailings used to generate the data and the parameters estimated using those data.

258 *2.3.2 Parameter estimation*

259 The values of many model parameters in the system of equations (3) are not available in the
260 literature, including the initial microbial biomass in OSTP and EPL (B(0)), the nitrogen half-
261 saturation constant (K_f), the half-saturation constants of the biodegradable hydrocarbons (K_{gi})
262 and λ_i. Because these parameters are related to the biodegradation module, we fit the
263 biodegradation module (system of equations (2)) to data obtained from laboratory biodegradation
264 studies cited above. To estimate these values, we used the nonlinear regression function *nlinfit(.)*
265 in MATLAB, which uses the Levenberg-Marquardt algorithm (Moré, 1978), to fit the solution of
266 the biodegradation module to the data. We provided the function with empirical data (see Table 2
267 for sources), the time points at which the data were collected (X), our simulated results at X, and
268 a random initial guess of parameter values. The system was integrated by calling a function that
269 takes as input the initial parameter values, the time at which the empirical data were collected,
270 and for any given time X uses the MATLAB function *ode15s(.)* to perform the integration. The
271 solution of the system obtained from the function was then evaluated at X, using the MATLAB
272 function *deval(.).* We also estimated the 95% confidence intervals of the predicted values by
273 using the MATLAB function *nlparci(.)*. To achieve this, we provided this function with the
274 coefficient estimates, residuals and the estimated coefficient covariance matrix from *nlinfit(.)*.
275 Some of the microbial model parameters used in the simulation, namely μ, r, and θ, were taken

from the literature: the units, values and source of these parameters are provided in Table S2. We assume here that no microbes died during laboratory incubation; thus, in fitting the data to our model, we take d to be zero.

2.3.3 Model validation against laboratory data

The new stoichiometric model was then validated against CH_4 production data generated in independent but parallel laboratory studies that measured biodegradation of paraffinic diluent in CNUL MFT (Mohamad Shahimin and Siddique, 2017a) and naphtha in Syncrude (Table S1) and CNRL MFT (Mohamad Shahimin and Siddique, 2017b). To this end, the concentrations of the labile hydrocarbons initially present in each diluent were used in the model to predict CH_4 production (Table S7). These predictions were compared with measured CH_4 produced by those tailings in independent laboratory experiments using the *goodnessOfFit(.)* function in MATLAB. As input, we provided this function with our test data, the simulated data from our model, and a cost function that determines the goodness of fit. We used the Normalized Mean Square Error (NMSE) function for this statistic, computed as

$$\text{NMSE} = 1 - \frac{\|[\text{actual}]-[\text{predicted}]\|^2}{\|[\text{actual}]-[\text{mean of actual}]\|^2},$$

where $\|.\|$ indicates the 2-norm of a vector, *predicted* is the output simulated by our model, *actual* is the input test data and *mean of actual* is the mean of the test data. $\text{NMSE} \in [-\infty, 1]$ where -∞ indicates a bad fit and 1 a perfect fit.

2.4 Quantitative comparison of model prediction and in-situ *measurement of CH_4 emissions from OSTP*

To further validate the applicability of model for predicting in-situ CH_4 emissions, we used (1) a modeling approach where kinetics of CH_4 production were estimated to determine the duration of CH_4 emissions, and (2) a direct approach that yielded a ballpark value of potential CH_4

299 emissions. For both approaches, we estimated the total mass of diluent entrained in froth
300 treatment tailings entering Syncrude MLSB, CNRL Horizon and CNUL MRM OSTPs in 2016
301 and 2017 (Table S6) and estimated the mass of individual biodegradable hydrocarbons in diluent
302 (Table S7) using published diluent compositions. To employ the modeling approach, we
303 assumed that these masses of individual hydrocarbons were present at the start of each year (i.e.,
304 the model was run as if all the diluent was introduced on January 1 of the year), while
305 acknowledging the continuous input of similar amounts of diluents in the years preceding 2016.
306 Using the estimated parameter values in Table S4, we modeled CH_4 production and calculated
307 the predicted cumulative CH_4 produced by metabolism of the constituent hydrocarbons over 366
308 days. The model output was compared with cumulative CH_4 emissions measured in flux
309 chambers at the surface of OSTP as reported to the Government of Alberta (unpublished; raw
310 data available upon request) (Table S8). Notably, surface flux measurements of CH_4 are not yet
311 available for the single EPL that was established in 2013, so the current comparison is limited to
312 OSTP measurements. In the direct approach, theoretical CH_4 production was estimated from the
313 masses of individual hydrocarbons biodegraded to methane using stoichiometric equations as
314 described in Table S8.

315 *2.5 Qualitative assessment of model predictions for OSTP and EPL*

316 In addition to quantitative analyses, the model was also qualitatively challenged to predict the
317 trajectories of CH_4 generation from OSTP (continuous $C_i^{in}>0$) versus EPL ($C_i=0$) under
318 hypothetical scenarios of carbon or nitrogen availability in-situ. Phase plane analysis was
319 performed (Supplemental Material section S3) by assuming that the diluent comprises C_i,
320 i=1,2,3…,18 are identical and sum up to C_T, and that the rate input of all the C_i per unit time

into the system is C_T^{in}. Equations were solved for microbial biomass versus total carbon content under eight combinations of C_i and N_A limitation over time.

The mathematical model and code are available at http://www.judekong.ca/publication/2019-05-01-Methanebiogenesismodel or from the authors upon request.

3. Results and Discussion

Previous zero- and first-order CH_4 production models from oil sands tailings (Siddique et al., 2008) used the available limited experimental data for diluent biodegradation and CH_4 production from four short-chain *n*-alkanes and four monoaromatic compounds during <1 year incubation with MFT from a single OSTP (Siddique et al., 2007, 2006). Those first approximation models assumed that organic carbon was the sole limiting nutrient in-situ and that microbial biomass was constant in OSTP despite receiving continuous and consistent inputs of diluent in froth treatment tailings. The stoichiometric model described here accounts for additional parameters including recently published biodegradation kinetics and CH_4 measurements for 18 relevant hydrocarbons including additional *n*-alkanes and, for the first time, *iso*-alkanes, incubated for much longer (up to 6.5 years) with MFT from three different OSTP impacted by distinct diluents. These additional experimental data allow the estimation of some kinetic parameters not previously considered and enable the new model to account for more biological factors than the previous models, so as to be adaptable to future modeling of in-situ CH_4 production from OSTP and EPL.

3.1 Data fitting to biodegradation and methane generation modules.

The biodegradation module was evaluated by fitting system of equations (2) to published experimental data sets for the 18 labile hydrocarbons listed in Table 2. Figures S3-S5 show the simulated biodegradation of diluent *n*-alkanes, monoaromatics and *iso*-alkanes compared with

344 measured biodegradation of these components. We obtained goodness-of-fit statistics (NMSE)
345 ranging from 0.85-1.00 (Table S3). These statistics show that the performance of the module
346 with respect to the training data is good.

347 To integrate the methane generation module with the biodegradation module, only three
348 model parameters were available in the literature (Table S2); others had to be estimated from
349 experimental data (Tables 2 and S4). Using these calculated values we applied the full
350 stoichiometric model to methane measurements from a suite of experiments analogous to but
351 independent of those used to estimate the parameters. Specifically, the CH_4 measurements were
352 acquired during long-term incubation of MFT samples from Syncrude, CNUL and CNRL with
353 their cognate diluents (Table S1, Siddique et al., 2015, Mohamad Shahimin and Siddique, 2017a,
354 respectively). Figure 1 shows that the model predicted methane generation very well for all three
355 types of MFT over long incubation times (> 4 yr incubation for CNUL and CNRL cultures).
356 Additional modeling of Syncrude MFT with mixtures of *n*-alkane or monoaromatic components
357 of its diluent (rather than whole diluent) also showed very good methane prediction (Fig. S6).

358 *3.2 Model evaluation and comparison to previous models*

359 Goodness-of-fit analysis of the stoichiometric model was calculated using NMSE (Table 3) that
360 showed excellent fit, ranging from 0.81 – 0.98 for the three combinations of MFT and diluent.
361 These NMSE results indicate that the integrated biodegradation and CH_4 production modules
362 rightly capture the behaviour of independent laboratory cultures and that the stoichiometric
363 model is sufficiently flexible to accommodate different inocula and substrates over long
364 incubation periods.

365 The new stoichiometric model was then compared with the previous zero- and first-order
366 kinetic models, as performed previously (Siddique et al., 2008), using the current data set. To

Commented [ST1]: Jude: In the response to reviewers' comments (Comment 10 under Reviewer 1), you mentioned Mohamad Shahimin and Siddique 2017b (paraffinic solvent with CNUL MFT) to validate your model but here you are citing Siddique et al. 2015 which is about individual paraffinic components with CNUL MFT. We need to correct it. I think you validated your model using 2017b data (whole paraffinic biodegradation) and you used 2015 paper for variable development, particularly 2-methylpentane and n-pentane as far as I remember.

this end, we first estimated the zero- and first-order kinetic model-related parameter values for the labile hydrocarbons that were not considered by Siddique et al. (2008) (Table S5). Figures 1 and S6, and Table 3 show that the stoichiometric model provides improved predictions over the previous models for describing CH_4 biogenesis from Syncrude MFT and whole naphtha or its components, and is far superior (matching closely with the measured methane) to the simpler models for the CNUL MFT–paraffinic diluent and for CNRL–naphtha combinations, neither of which were available for the previous modeling study. The improved fit regarding lag time and extent of CH_4 production, and the improved NMSE values suggest that the stoichiometric model, which is based on laboratory cultures, would be useful for modeling in-situ CH_4 production from different OSTP and EPL.

3.3 Quantitative comparison of stoichiometric model predictions to measured cumulative CH_4 field emissions

To evaluate the feasibility of applying this model based on laboratory cultures to field emissions of CH_4, we compared the reported measured volumes of CH_4 emitted from the surfaces of OSTPs with cumulative CH_4 masses predicted by our model. Table 4 shows the comparison between the reported measured methane emissions from OSTPs in 2016 and 2017 and the maximum theoretical CH_4 yield predicted by our model based on the estimated diluent entering OSTPs (Table S6) for 2016 and 2017. The stoichiometric model predictions are 50-55 % of the measured emissions from Syncrude MLSB and 77-95% of the measured emissions from CNRL OSTP in both years. For CNUL where paraffinic solvent is used, the model predictions were 48% of the measured emissions in 2017 but only 17% of the emissions in 2016. This latter difference may be attributed to markedly greater methane emission data from CNUL OSTP reported in 2016 compared to all other OSTPs (Tables 4 and S5). The overall trend is very clear

that the model predicted about 50% of emissions from Syncrude and CNUL OSTP and >75% of emissions from CNRL OSTP. This likely reflects the diluent compositions, with only ~40% of fugitive Syncrude and CNRL naphtha diluent being considered labile versus ~60% of CNUL paraffinic diluent, based on the mass of known biodegradable hydrocarbons in the diluents (Table S7).

This difference between predicted and measured CH_4 masses suggests that (other than possible inaccuracies associated with field measurements) there are other endogenous carbon sources present in OSTP that support methanogenesis but are not currently accounted for by the model. Such possible sources include (but are not limited to): (1) additional labile diluent hydrocarbons not yet identified in our laboratory incubations and therefore not included in the model; (2) recalcitrant hydrocarbons deposited in previous years (and therefore not included in the annual C_i^{in} model input) that are slowly degraded as the community adapts to residual naphtha after depletion of the labile hydrocarbons in lower strata, e.g., some *iso*-alkanes and cycloalkanes having extremely long lag times or slow degradation rates (e.g., Abu Laban et al., 2015); (3) slowly-degradable metabolites produced historically during incomplete biodegradation of hydrocarbon or from non-hydrocarbon carbon substrates; (4) organic matter associated with clays in oil sands ores (Sparks et al., 2003); (5) minor labile components of bitumen e.g., high molecular weight *n*-alkanes (Oberding and Gieg, 2018); and (6) organic additives used in ore processing and deposited with tailings, e.g., citrate that is used as an amendment in some OSTPs (Foght et al., 2017) and is a potentially large source of unaccounted CH_4 in CNUL MRM. Another explanation for larger masses of measured emissions is the delayed, stochastic release of methane produced years ago from labile HCs that is 'trapped' in lower strata of MFT (Guo, 2009) until (1) suitably-sized and -oriented channels are created (e.g.,

by microbial activity, Siddique et al., 2014) and/or (2) cumulative gas voids reach critical buoyancy and rise from deep tailings, and/or (3) MFT strata are disturbed by some physical activity in the pond (e.g., moving deposition pipes, transferring MFT to new pits, etc.) allowing escape of gas.

There is an agreement between the model predictions and measured field emissions despite the obvious reasons of discrepancy discussed above. However, additional qualitative factors must be addressed to expand the developed model to in-situ predictions while keeping in mind the inherent differences between laboratory cultures and field operations: (1) cultures are incubated with a single input of hydrocarbons, i.e., in "batch mode" with finite C_i^{in}, whereas the upper strata of OSTP receive ongoing input of diluent, i.e., "continuous mode" where $C_i^{in} > 0$. The laboratory cultures are more analogous to EPL, where $C_i^{in} = 0$ or to the lower strata of OSTP to which fresh diluent deposited at the surface cannot effectively diffuse and where, essentially, $C_i^{in} = 0$. (2) As discussed above, anaerobic biodegradation kinetics are currently available for only 18 hydrocarbons in cultures, whereas additional constituents of whole diluent and possibly a small subset of bitumen constituents may be susceptible to biodegradation in-situ. Restriction of the parameter C_i to the current 18 hydrocarbons would likely cause the model to under-estimate methane production in-situ. Selective depletion of naphtha constituents with depth in OSTP has been observed qualitatively (Figure S2 in Foght et al., 2017) and such information could be used in future to expand the substrate range of the stoichiometric model and better represent in-situ biodegradation. (3) The model currently includes a variable for lag time (λ), the time elapsed between addition of hydrocarbon and appearance of measureable CH_4. In fact, lag times of 5-15 years were observed between the inauguration of OSTP and the first observation of ebullition at the pond surface (Foght et al., 2017), likely reflecting the time required for establishment of

436 efficient methanogenic communities. However, this variable is likely relevant only to laboratory
437 studies, due to disruption of the microbial consortia during initiation of the cultures, and to newly
438 established OSTP and EPL when transfer of tailings begins. After onset of CH_4 production,
439 OSTP subsequently do not exhibit any apparent lag phases because of continuous diluent input
440 and λ=0 in-situ. (4) Small scale culture bottles facilitate release of CH_4 from MFT to the
441 headspace for measurement compared with static deep strata in OSTP and EPL that experience
442 physical retention of GHG as methane voids (Guo, 2009). That is, the model predicts CH_4
443 production based on 100% release from MFT; the proportion of gas released to the pond surface
444 versus that retained under hydraulic pressure in-situ is not a component of the model. (5)
445 Methanogenesis depends completely upon the microbial community composition, which is
446 complex (An et al., 2013) and specific to each OSTP and EPL (Wilson et al., 2016), and may
447 diverge from cultured communities during incubation. Although some diversity data exist both
448 for cultures and various MFT, the model does not include parameters to account for the presence
449 or abundance of 'keystone' microbial species because, in tailings, such species currently are
450 incompletely known or identified. Significant efforts in research and testing would be required to
451 integrate microbial community analysis into any CH_4 model for oil sands operations. (6) Finally,
452 the model does not currently include parameters that reflect potential changes to ore processing
453 or OSTP practices such as subtle alterations in diluent composition, intermittent deposition of
454 chemicals from related processes (e.g., ammonium; Foght et al., 2017), changes in froth
455 treatment water temperature, etc.

456 *3.4 Qualitative test of model prediction*

457 Despite the inferred shortcomings of applying the model to field predictions, and in anticipation
458 of acquiring in-situ measurements to provide parameters for use in future for field modeling, it is

459 possible to conduct a qualitative test of the stoichiometric model to determine whether it predicts
460 expected trajectories under different expected field scenarios, e.g., limiting C_T and/or N_A
461 conditions. Whereas cultures receive hydrocarbons in excess of instantaneous microbial demand
462 at the beginning of incubation, as do the upper strata of active OSTP, labile carbon may become
463 limiting in lower (older) strata of OSTP and eventually in EPL and cultures, where diluent is not
464 replenished. Similarly, cultures initially receive a very small but finite amount of soluble
465 nitrogen and have a headspace of N_2 gas (which may serve as a nitrogen source for tailings
466 microbiota; Collins et al., 2016) but the lower strata of OSTP and EPL have no obvious input of
467 biologically available nitrogen (N_A). Therefore this nutrient (or others, currently unidentified)
468 may become limiting with time. Thus, challenging a model developed using culture data with
469 scenarios reflecting in-situ conditions should reveal the strength of the model. Phase plane
470 analyses of eight forms of potential solutions of the stoichiometric model are shown in Figures
471 S7 and S8 and described in Supplemental Material section S3. The model outputs describe the
472 expected trajectories of OSTP and EPL under carbon and/or nitrogen limitation, solving for
473 biomass and total carbon in the system with time, i.e., the sum of all microbial activity in-situ.
474 The predicted behaviour of OSTP with continuous diluent input differs from EPL with no
475 additional hydrocarbon input, and the effect of limiting nutrient (nitrogen) also changes the
476 ultimate endpoints of biomass and carbon in the two scenarios. These outputs qualitatively
477 support the validity of the model as well as indicating that the stoichiometric model could be
478 used to predict specific OSTP and EPL behaviour, to predict the volumes of 'legacy' CH_4 from
479 OSTP and long-term duration of CH_4 production in-situ (particularly from EPL), and to
480 influence decisions about oil sands reclamation strategies. If additional in-situ model parameters
481 are acquired, the model can be further refined to improve predictive power.

4. Conclusions

The stoichiometric model represents a significant advance over previous zero- and first-order kinetic models, particularly because it predicts well the GHG emissions from different operators using distinct diluents that may support different rates of CH_4 production or may ultimately generate greater CH_4 emissions. Application of the model to in-situ CH_4 production is still hampered by limited experimental data and field measurements; some of these gaps may be alleviated as relevant in-situ data are acquired and when future anaerobic studies provide both evidence for susceptibility of additional hydrocarbons to biodegradation and more precise values for model parameters. The model is sufficiently flexible that additional parameters can be added to the modules as laboratory or field data become available. Until such time, the stoichiometric model should assist regulators and oil sands operators in qualitatively assessing long-term GHG emissions from oil sands tailings deposits and EPL reclamation sites.

Appendix A. Supplementary Material

This manuscript is accompanied by Supplementary Material comprising stability analysis of our System, eight tables (Tables S1-S8) and eight figures (Figure S1-S8).

ACKNOWLEDGMENTS

We acknowledge support from NSERC Discovery Grants (TS, JF, HW and MAL), Canada Foundation for Innovation (128377; TS), NSERC Postdoctoral Fellowship (#PDF-502490-2017; JK) and a Canada Research Chair (MAL). In addition, JK thanks DIMACS for providing space to conduct the analyses (partially enabled through support from the National Science Foundation under grant #CCF-1445755.).

Disclaimer: Government of Alberta neither approves nor disapproves this publication.

REFERENCES

Abu Laban, N., Dao, A., Semple, K., Foght, J., 2015. Biodegradation of C_7 and C_8 iso-alkanes under methanogenic conditions. Environ. Microbiol. 17, 4898–4915.

Alberta Energy Regulator, 2019. Electronic resource about oil sands [WWW Document]. URL https://www.aer.ca (accessed 7.10.19).

Alberta Greenhouse Gas Report, 2016. Alberta Greenhouse Gas Reporting Program 2012 Facility Emissions. Available at: https://open.alberta.ca/dataset/9b11d727-06be-4ade-9ad9-cfea1a559103/resource/43aeec2e-b22f-4cf4-9e1b-561aad633ee8/download/2012reportgreenhousegasemissions-sep2016.pdf (accessed May 02, 2019)

An, D., Caffrey, S.M., Soh, J., Agrawal, A., Brown, D., Budwill, K., Dong, X., Dunfield, P.F., Foght, J., Gieg, L.M., Hallam, S.J., Hanson, N.W., He, Z., Jack, T.R., Klassen, J., Konwar, K.M., Kuatsjah, E., Li, C., Larter, S., Leopatra, V., Nesbø, C.L., Oldenburg, T., Pagé, A.P., Ramos-Padron, E., Rochman, F.F., Saidi-Mehrabad, A., Sensen, C.W., Sipahimalani, P., Song, Y.C., Wilson, S., Wolbring, G., Wong, M.-L., Voordouw, G., 2013. Metagenomics of Hydrocarbon Resource Environments Indicates Aerobic Taxa and Genes to be Unexpectedly Common. Environ. Sci. Technol. 47, 10708–10717. https://doi.org/10.1021/es4020184

Burkus, Z., Wheler, J., Pletcher, S., 2014. GHG emissions from oil sands tailings ponds: Overview and modelling based on fermentable substrates. Alberta Environment and Sustainable Resource Devevelopment. November 2014 https://doi.org/10.7939/R3F188

Charette, T., Castendyk, D., Hrynyshyn, J., Kupper, A., McKenna, G., Mooder, B., 2012. End Pit Lakes Guidance Document 2012. Cumulative Environmental Management Association Fort

McMurray, Alberta, Canada 2010. http://library.cemaonline.ca/ckan/dataset/2010-0016/resour ce/1632ce6e-d1a0-441a-a026-8a839f1d64bc (accessed 4.28.19).

Collins, C.E.V., 2013. Methane Production in Oil Sands Tailings under Nitrogen-Depleted Conditions. Master's thesis. University of Alberta.

Collins, C.E.V., Foght, J.M., Siddique, T., 2016. Co-occurrence of methanogenesis and N 2 fixation in oil sands tailings. Sci. Total Environ. 565, 306–312.

Foght, J.M., Gieg, L.M., Siddique, T., 2017. The microbiology of oil sands tailings: Past, present, future. FEMS Microbiol. Ecol. 93 (5), fix034 https://doi.org/10.1093/femsec/fix034

Government of Alberta, 2019a. Electronic resource about oil sands [WWW Document]. URL https://www.energy.alberta.ca/OS/AOS/Pages/default.aspx (accessed 4.24.19).

Government of Alberta, 2019b. Oil Sands Information Portal [WWW Document]. URL http://osip.alberta.ca/map/ (accessed 7.14.19).

Guo, C., 2009. Rapid densification of the oil sands mature fine tailings (MFT) by microbial activity. PhD thesis, University of Alberta. https://doi.org/10.7939/R3K988

Makino, W., Cotner, J.B., Sterner, R.W., Elser, J.J., 2003. Are bacteria more like plants or animals? Growth rate and resource dependence of bacterial C: N: P stoichiometry. Funct. Ecol. 17, 121–130.

Mohamad Shahimin, M.F., Foght, J.M., Siddique, T., 2016. Preferential methanogenic biodegradation of short-chain n-alkanes by microbial communities from two different oil sands tailings ponds. Sci. Total Environ. 553, 250–257.

Mohamad Shahimin, M.F., Siddique, T., 2017a. Methanogenic biodegradation of paraffinic solvent hydrocarbons in two different oil sands tailings. Sci. Total Environ. 583, 115–122.

Mohamad Shahimin, M.F., Siddique, T., 2017b. Sequential biodegradation of complex naphtha

hydrocarbons under methanogenic conditions in two different oil sands tailings. Environ. Pollut. 221, 398–406.

Moré, J.J., 1978. The Levenberg-Marquardt algorithm: implementation and theory. In G. A. Watson, (Ed.), *Numerical Analysis*, Lecture Notes in Mathematics 630. Springer, pp. 105–116.

Oberding, L.K., Gieg, L.M., 2018. Methanogenic paraffin biodegradation: alkylsuccinate synthase gene quantification and dicarboxylic acid production. Appl. Environ. Microbiol. 84(1), e01773-17. https://doi.org/10.1128/AEM.01773-17.

Penner, T.J., Foght, J.M., 2010. Mature fine tailings from oil sands processing harbour diverse methanogenic communities. Can. J. Microbiol. 56, 459–470. https://doi.org/10.1139/W10-029

Risacher, FF; Morris, PK; Arriagaa, D.; Goada, C; Colenbrander Nelson, T.; Slater, GF; Warren, LA. 2018. The interplay of methane and ammonia as key oxygen consuming constituents in early stage development of Base Mine Lake, the first demonstration oil sands pit lake. Appl. Geochem. 93, 49–59 https://doi.org/10.1016/j.apgeochem.2018.03.013

Roberts, D.J., 2002. Methods for assessing anaerobic biodegradation potential. In: Hurst, C.J., Crawford, R.L., Knudson, G.R., McInerney, M.J., Stetzenbach, L.D. (Eds.), Manual of Environmental Microbiology, second ed. ASM Press, USA, pp.1008–1017.

Siddique, T., Fedorak, P.M., Foght, J.M., 2006. Biodegradation of short-chain n-alkanes in oil sands tailings under methanogenic conditions. Environ. Sci. Technol. 40, 5459–5464.

Siddique, T., Fedorak, P.M., MacKinnon, M.D., Foght, J.M., 2007. Metabolism of BTEX and naphtha compounds to methane in oil sands tailings. Environ. Sci. Technol. 41, 2350–2356.

Siddique, T., Gupta, R., Fedorak, P.M., MacKinnon, M.D., Foght, J.M., 2008. A first

573 approximation kinetic model to predict methane generation from an oil sands tailings
574 settling basin. Chemosphere 72, 1573–1580.
575 Siddique, T., Kuznetsov, P., Kuznetsova, A., Arkell, N., Young, R., Li, C., Guigard, S.,
576 Underwood, E., Foght, J.M., Raymond, J., Grunden, A.M., 2014. Microbially-accelerated
577 consolidation of oil sands tailings. Pathway I: changes in porewater chemistry. Front.
578 Microbiol. 5, 106. https://doi.org/10.3389/fmicb.2014.00106
579 Siddique, T., Mohamad Shahimin, M.F., Zamir, S., Semple, K., Li, C., Foght, J.M., 2015. Long-
580 term incubation reveals methanogenic biodegradation of C_5 and C_6 iso-alkanes in oil sands
581 tailings. Environ. Sci. Technol. 49, 14732–14739.
582 Siddique, T., Penner, T., Semple, K., Foght, J.M., 2011. Anaerobic biodegradation of longer-
583 chain *n*-alkanes coupled to methane production in oil sands tailings. Environ. Sci. Technol.
584 45, 5892–5899.
585 Siddique, T., Stasik, S., Mohamad Shahimin, M.F., Wendt-Potthoff, K., 2018. Microbial
586 communities in oil sands tailings: their implications in biogeochemical processes and
587 tailings management. Springer Nat. Switz. AG 2018 T. J. McGenity (ed.), Microbial
588 Communities Utilizing Hydrocabons and Lipids: Handbook of Hydrocarbon and Lipid
589 Microbiology, 2nd edn. Springer, Cham, 1-33.
590 Sparks, B.D., Kotlyar, L.S., O'Carroll, J.B., Chung, K.H., 2003. Athabasca oil sands: effect of
591 organic coated solids on bitumen recovery and quality. J. Pet. Sci. Eng. 39, 417–430.
592 Sterner, R.W., Elser, J.J., 2002. Ecological stoichiometry: the biology of elements from
593 molecules to the biosphere. Princeton University Press.
594 Symons, G.E., Buswell, A.M., 1933. The methane fermentation of carbohydrates1, 2. J. Am.
595 Chem. Soc. 55, 2028–2036.

596 Wilson, S.L., Li, C., Ramos-Padrón, E., Nesbø, C., Soh, J., Sensen, C.W., Voordouw, G., Foght,
597 J., Gieg, L.M., 2016. Oil sands tailings ponds harbour a small core prokaryotic microbiome
598 and diverse accessory communities. J. Biotechnol. 235, 187–196.
599 https://doi.org/10.1016/j.jbiotec.2016.06.030
600

Table 1: Definition of terms used in model development

Term	Definition
C_i	mass of individual labile hydrocarbons in the system, where i=1…n, assuming n labile hydrocarbons in system *
C_i^{in}	mass of C_i inflow to the system
C_T	total mass of labile (biodegradable) hydrocarbon in the system (i.e., the sum of all C_i)
μ	specific microbial growth rate of microbes (bacteria and archaea) supported by C_T
μ_i	specific microbial growth rate supported by each labile hydrocarbon C_i
N_T	total mass of nitrogen in the system
N_A	mass of N_T that is biologically available §
B	total biomass of living microbes
b	biomass of dead microbes
β_i	the proportion of C_i contained in dead biomass that is available for microbial recycling
θ	the ratio of nitrogen to carbon associated with microbial biomass B
r	proportionality constant defining efficiency of conversion of C_T to B
r_i	proportionality constant defining efficiency of conversion of each C_i to B; r_i = B / C_i consumed
λ_i	lag period before the onset of biodegradation of each C_i
d	microbial cell death rate
K_f	N_A-dependent half-saturation constant
K_{gi}	C_i-dependent half-saturation constant
Γ_i	expected yield of CH_4 from biodegradation of one mole of C_i
G_i	Total CH_4 and CO_2 generated from the biodegradation of C_i
η	fraction of sum of Γ_i for all i, yielded by biodegradation of C_T; i.e., methane bioconversion efficiency factor
η_i	fraction of Γ_i yielded by biodegradation of each C_i

*, in developing the current model, we considered 18 specific hydrocarbons present in naphtha and paraffinic diluents (see Table 2)

§, e.g., nitrate, nitrite, ammonium, dinitrogen (N_2 gas), labile organic N compounds (e.g., macromolecules in biomass), but not complex molecules (e.g., resins found in bitumen)

Table 2: List of 18 labile diluent hydrocarbons used in model development, sources of data and type of tailings used to generate data for the biodegradation module and to estimate model parameter values, and the model parameters estimated using those data (see Table S4 for parameter definitions and values).

Hydrocarbon	Source of data	Type of tailings	Parameters estimated from the data
n-Alkanes			
C_5	Mohamad Shahimin et al. (2016)	CNUL	$K_{g_{C_5}}$ and C_5-lag
C_6, C_7, C_8, C_{10}	Siddique et al. (2006)	Syncrude	B(0), K_f, N_T, $K_{g_{C_6}}$, $K_{g_{C_7}}$, $K_{g_{C_8}}$, $K_{g_{C_{10}}}$, C_6-lag, C_7-lag, C_8-lag and C_{10}-lag.
C_9	Table S1	Syncrude	$K_{g_{C_9}}$ and C_9-lag
iso-Alkanes *			
2-MC_6§, 3-MC_6, 2-MC_7, 4-MC_7, 2-MC_8, 3-MC_8§, 2-MC_9§,	Siddique et al., unpublished	Syncrude	$K_{g_{3-MC_6}}$, $K_{g_{2-MC_7}}$, $K_{g_{4-MC_7}}$, $K_{g_{2-MC_8}}$, 3-MC_6 –lag, 2-MC_7-lag , 4-MC_7-lag, and 2-MC_8-lag
2-MC_5	Mohamad Shahimin and Siddique (2017a)	CNUL	$K_{g_{2-MC_5}}$ and 2-MC_5-lag
Monoaromatics			
Toluene, *o*-Xylene, *m*- plus *p*-Xylene	Siddique et al. (2007)	Syncrude	$K_{g_{toluene}}$, $K_{g_{o-xylene}}$, $K_{g_{mp-xylene}}$, toluene-lag, *o*-xylene-lag, and *m,p*-xylene-lag

* M denotes a methyl group; i.e., 2-MC_6 is 2-methylhexane, etc. See Methods section 2.3.1 for full list of abbreviations

§ The values of model parameters K_g and lag for 2-MC_6, 3-MC_8 and 2-MC_9 are not available from empirical studies and are assumed to be the same as those for 3-MC_6, 2-MC_8 and 2-MC_8, respectively, due to their similar molecular weights.

Table 3: Normalized mean square error (NMSE) analysis of model predictions and measured CH_4 production from laboratory cultures comprising three MFT samples incubated with their cognate diluents. The zero- and first-order models were implemented as described by Siddique et al. (2008) using data reported in the current study. See Figures 1 and S6 for graphical comparison of model outputs.

	NMSE values		
	MFT source and diluent type		
	Syncrude	**CNUL**	**CNRL**
Model	**Naphtha diluent**	**Paraffinic diluent**	**Naphtha diluent**
Zero-order	-0.28	-1.00	-1.10
First-order	-0.65	0.82	0.61
Stoichiometric	0.81	0.98	0.97

623 **Table 4:** Comparison of cumulative field measurements of CH_4 emissions in 2016 and 2017 in
624 three OSTP versus stochiometric model predictions of cumulative in-situ CH_4 emissions from
625 those OSTP.

Operator and OSTP (date)	Field measurements of CH_4 emissions (moles x 10^6) *	Stochiometric model predictions of methane emissions (moles x 10^6)	Proportion of field emissions predicted by model (%) §
Syncrude MLSB (2016)	1191	656	55
Syncrude MLSB (2017)	991	492	50
CNRL Horizon (2016)	336	321	95
CNRL Horizon (2017)	599	459	77
CNUL MRM (2016)	2634	445	17
CNUL MRM (2017)	1051	506	48

626 * Unpublished surface flux measurements (Government of Alberta; raw data available upon
627 request), reported as tonnes and converted to moles at standard temperature and pressure

628 § for detailed calculations see Table S8

629 **FIGURE LEGEND**

630 **Figure 1**: Comparison of CH_4 production predicted by the stoichiometric model versus CH_4
631 measured in laboratory cultures independent of those used to generate the stoichiometric model
632 and parameters (Table S4). Methane measurements (diamond symbols) are from cultures
633 comprising: (A), Syncrude MFT incubated with its naphtha diluent (B), CNUL MFT incubated
634 with its paraffinic diluent; and (C), CNRL MFT incubated with its naphtha diluent. Solid lines
635 represent the stoichiometric model prediction; dashed lines and dotted lines respectively
636 represent predictions made by applying the previous zero-order and first-order models
637 (Siddique et al., 2008) to the independent data set. The parameters values used in simulating
638 the zero-order and first-order models were obtained from Siddique et al. (2008) and Table S5.

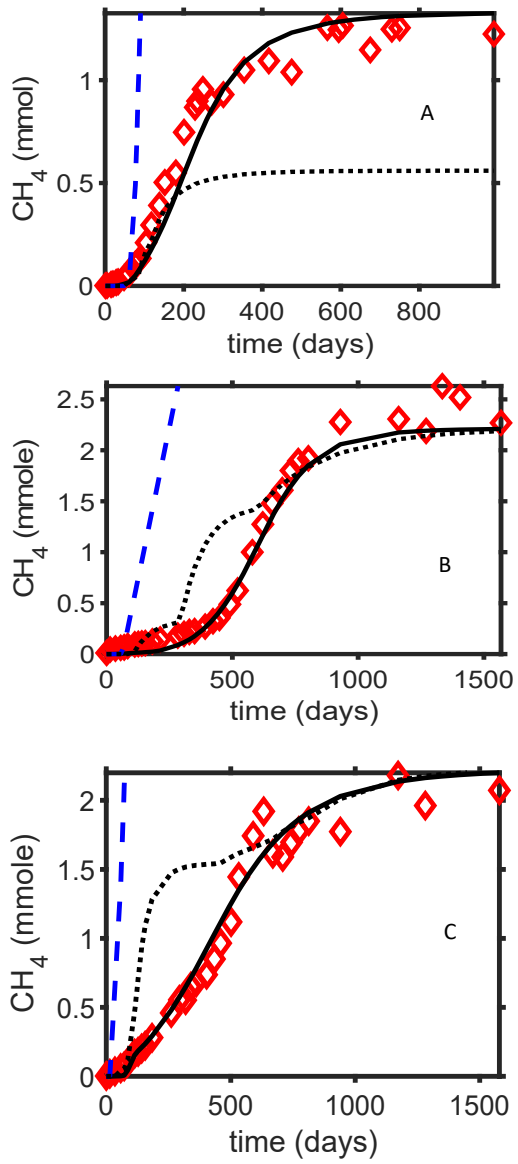
CH4 (mmol)
time (days)
A
CH4 (mmole)
time (days)
B
CH4 (mmole)
time (days)
C

Figure: 1

Appendix A:

Second-generation stoichiometric mathematical model to predict methane emissions from oil sands tailings

Jude Kong[1,2], Hao Wang[2*†], Tariq Siddique[3*‡], Julia Foght[4], Kathleen Semple[4], Zvonko Burkus[5], and Mark Lewis[2,4]

[1]Center for Discrete Mathematics and Theoretical computer Science, Rutgers University, 96 Frelinghuysen Road Piscataway, NJ 08854-8018, USA

[2]Department of Mathematical and Statistical Sciences, University of Alberta, Edmonton, AB T6G 2G1, Canada

[3]Department of Renewable Resources, University of Alberta, Edmonton, AB T6G 2G7, Canada

[4]Department of Biological Sciences, University of Alberta, Edmonton, AB T6G 2E9, Canada

[5]Alberta Environment and Parks, Government of Alberta, Edmonton, Canada

Corresponding authors' emails:

[*†] Mathematical approach (Hao Wang); hao8@ualberta.ca

[*‡] Biological approach (Tariq Siddique); tariq.siddique@ualberta.ca

The following Supplementary Material contains the mathematical analysis of the system of equations (2), eight tables (Tables S1- S8) and eight figures (Figures S1-S8).

S1. Brief description of MFT laboratory culture methods used to generate data for model development and testing

Details of laboratory culture preparation can be found in published papers (Mohamad Shahimin et al., 2016; Mohamad Shahimin and Siddique, 2017a, 2017b, Siddique et al., 2007, 2006). Briefly and very generally, bulk samples of MFT were dispensed anaerobically into small serum bottles (microcosms) in replicate (typically triplicates) amended with an equal volume of sterile methanogenic medium comprising inorganic salts, trace vitamins, a redox indicator and sulfide as a reducing agent, but lacking organic carbon, and sealed under an atmosphere of 80% O_2-free N_2, balance CO_2. The microcosms were allowed to incubate stationary in the dark at room temperature (ca. 22°C) for 2 weeks to acclimate, then the headspace was flushed with O_2-free N_2 plus CO_2 to remove any CH_4 produced from endogenous substrates. The microcosms were then amended by injecting neat diluent supplied by the operator, or in one case defined mixtures of pure hydrocarbon constituents of the diluent (i.e., mixtures of *n*-alkanes or monoaromatics; Figure S6). During incubation headspace gases were sub-sampled at intervals for analysis by gas chromatography to determine cumulative CH_4 production. Likewise the MFT slurry was sub-sampled at intervals to analyze residual hydrocarbons using gas chromatography with mass spectrometry and thereby to calculate biodegradation by difference. Control microcosms containing MFT that had been heat-sterilized using an autoclave were included with each experiment to account for any abiotic losses of hydrocarbons.

S2. Model development details

S2.1 Mathematical analysis of the biodegradation module

Here, a basic mathematical analysis of the system of equations (2) is provided. First we let C_T to represent the sum of all the labile hydrocarbons in the system and the sum of all C_i^{in} to be C_T^{in}..

We assume that $\lambda_i = 0,$ for all i=1,2,3..n. This leads to a system of two differential equations.

To simplify our phase plane analysis in a meaningful way, we adjusted the second differential by introducing a new variable:

$A = \frac{B}{r} + C_T$. 'A' represents the sum of the total carbon available in the system and bacterial biomass. We assume that f, g are linear and find their linear approximations:

$$f(N_T - \theta B) \approx f(0) + f'(0)(N_T - \theta B)$$

$$\Longrightarrow f(N_T - \theta B) \approx \frac{N_T - \theta B}{K_f}$$

$$g\left(A - \frac{B}{r}\right) \approx g(0) + g'(0)\left(A - \frac{B}{r}\right)$$

$$\Longrightarrow g\left(A - \frac{B}{r}\right) \approx \frac{A - \frac{B}{r}}{K_g}$$

We thus have the following system in which only one of the two differential equations has a minimum function, greatly simplifying the analysis:

$$\dot{A} = \frac{r-1}{r} dB + C_T^{in} = F(B) \qquad \text{(S1)}$$

$$\dot{B} = \mu B min\left\{f(N_T - \theta B), g\left(A - \frac{B}{r}\right)\right\} - dB = BG(A, B).$$

Next, we look at the stability analysis of the system. For this purpose, we construct a phase plane of the system, (i.e. a graph of the solution trajectories mapped out by points *(A(t),B(t))* as t varies over (∞,+∞)) in order to identify the steady state solutions. We call $F(B) = 0$ and $G(A, B) = 0$ (the lines on which trajectories are horizontal or vertical) the nullclines of system of equations (S1). The steady state solutions are the points where the nullclines (but not different branches of the same nullcline) cross each other. For the stability of the steady states, we compute the Jacobian matrix corresponding to each equilibrium point $J(A^*, B^*)$, where (A^*, B^*) is a given

equilibrium point. We use the sign of the trace and determinant of $J(A^*, B^*)$ to determine the nature of the given equilibrium point. Let D = det $J(A^*, B^*)$ and T_r = trace $J(A^*, B^*)$. Note that:

1) If $D < 0$, the eigenvalues of J(A^*,B^*) are real and of opposite signs, and the phase portrait is a saddle (which is always unstable).

2) If $0 < D < \frac{T_r^2}{4}$, the eigenvalues of $J(A^*, B^*)$ are real, distinct, and of the same sign, and the phase portrait is a node, stable if $T_r < 0$ and unstable if $T_r > 0$.

3) If $0 < T_r^2 < D$, the eigenvalues of $J(A^*, B^*)$ are neither real nor purely imaginary, and the phase portrait is a spiral, stable if $T_r < 0$ and unstable if $T_r > 0$. Using this idea, we carried out the analysis as follows:

S2.2 Stability Analysis of OSTP system ($C_T^{in} \neq 0$)

Steady states:

A-Nullclines:

$\dot{A} = 0, \implies B = \frac{rC_T^{in}}{d(1-r)}$.

B-Nullclines:

$$\dot{B} = 0, \Longrightarrow B = 0 \; or \; G(A,B) = 0.$$

$$G(A,B) = 0, \Longrightarrow \begin{cases} B = Ar - \dfrac{dk_g r}{\mu} \; if \; \dfrac{N_T - \theta B}{k_f} > \dfrac{A - \dfrac{B}{r}}{k_g} \\ B = \left(N_T - \dfrac{dk_f}{\mu}\right)\dfrac{1}{\theta} \; if \; \dfrac{N_T - \theta B}{k_f} < \dfrac{A - \dfrac{B}{r}}{k_g} \end{cases}$$

Case 1: Suppose $\theta - \frac{k_f}{k_g r} > 0$, then

$$G(A,B)=0,\Longrightarrow \begin{cases} B=Ar-\dfrac{dk_g r}{\mu}\ if\ B<\left(N_T-\dfrac{Ak_f}{k_g}\right)\left(\dfrac{k_g r}{\theta k_g r-k_f}\right) \\ B=\left(N_T-\dfrac{dk_f}{\mu}\right)\dfrac{1}{\theta}\ if\ B>\left(N_T-\dfrac{Ak_f}{k_g}\right)\left(\dfrac{k_g r}{\theta k_g r-k_f}\right) \end{cases}$$

Case 1.1: If $C_T^{in}>\frac{d(1-r)}{r\theta}\left(N_T-\frac{dk_f}{\mu}\right)$, there will be no intersection between the A and B-nullclines as shown in Panel A of Figure S7. Hence the system will have no equilibrium point.

Case 1.2: If $C_T^{in}<\frac{d(1-r)}{r\theta}\left(N_T-\frac{dk_f}{\mu}\right)$, the two nullclines will intersect at one unique point $E_1=\left(\frac{\mu C^{in}+d^2k_g(1-r)}{d(1-r)\mu},\frac{rC_T^{in}}{d(1-r)}\right)$ as shown in Panel B of Figure S7. Hence if $C_T^{in}<\frac{d(1-r)}{r\theta}\left(N_T-\frac{dk_f}{\mu}\right)$, the system will have a unique internal equilibrium point E_1.

Case 1.3: If $C_T^{in}=\frac{d(1-r)}{r\theta}\left(N_T-\frac{dk_f}{\mu}\right)$, the two nullclines will intersect on the line $\left\{\left(A,\left(T-\frac{dk_f}{\mu}\right)\frac{1}{\theta}\right):A>\frac{1}{r}\left[\left(T-\frac{dk_f}{\mu}\right)\frac{1}{\theta}+\frac{dk_g r}{\mu}\right]\right\}$ as can be seen in Panel A of Figure S8. Consequently, If $C_T^{in}=\frac{d(1-r)}{r\theta}\left(N_T-\frac{dk_f}{\mu}\right)$, the system will have an infinite number of equilibrium points $E_2=\left\{\left(A,\left(N_T-\frac{dk_f}{\mu}\right)\frac{1}{\theta}\right):A>\frac{1}{r}\left[\left(N_T-\frac{dk_f}{\mu}\right)\frac{1}{\theta}+\frac{dk_g r}{\mu}\right]\right\}$

Case 2: Suppose $\theta-\frac{k_f}{k_g r}<0$, then

$$G(A,B)=0,\Longrightarrow \begin{cases} B=Ar-\dfrac{dk_g r}{\mu}\ if\ B>\left(N_T-\dfrac{Ak_f}{k_g}\right)\left(\dfrac{k_g r}{\theta k_g r-k_f}\right) \\ B=\left(N_T-\dfrac{dk_f}{\mu}\right)\dfrac{1}{\theta}\ if\ B<\left(N_T-\dfrac{Ak_f}{k_g}\right)\left(\dfrac{k_g r}{\theta k_g r-k_f}\right). \end{cases}$$

Note that the slope of the line $B = Ar - \frac{dk_g r}{\mu}$ is less than that of $B = \left(N_T - \frac{Ak_f}{k_g}\right)\left(\frac{k_g r}{\theta k_g r - k_f}\right)$, since $\frac{k_f}{k_f - \theta k_g r} > 1$. Therefore, the point where the line $B = Ar - \frac{dk_g r}{\mu}$ intersects the A-axis, $\frac{dk_g}{\mu}$, must be less than $\frac{Tk_g}{k_f}$, the point where the $B = \left(N_T - \frac{Ak_f}{k_g}\right)\left(\frac{k_g r}{\theta k_g r - k_f}\right)$ intersect the A-axis, for the two lines to intersect on the first quadrant.

Case 2.1: If $C_T^{in} > \frac{d(1-r)}{r\theta}\left(N_T - \frac{dk_f}{\mu}\right)$, as with Case 1.1, there will be no intersection between the A and B-nullclines as shown in Panel B of Figure S8. Hence the system will have no equilibrium point.

Case 2.2: $C_T^{in} < \frac{d(1-r)}{r\theta}\left(N_T - \frac{dk_f}{\mu}\right)$, the two nullclines will intersect at one unique point $E_3 = \left(\frac{\mu C^{in} + d^2 k_g (1-r)}{d(1-r)\mu}, \frac{r C_T^{in}}{d(1-r)}\right)$ as shown in Panel C of Figure S8. Hence if $\theta\ C_T^{in} < \frac{d(1-r)}{r\theta}\left(N_T - \frac{dk_f}{\mu}\right)$, the system will have a unique internal equilibrium point E_3.

Case 2.3: If $C_T^{in} = \frac{d(1-r)}{r\theta}\left(N_T - \frac{dk_f}{\mu}\right)$, the two nullclines will intersect on the line $\left\{\left(A, \left(N_T - \frac{dk_f}{\mu}\right)\frac{1}{\theta}\right) : A > \frac{1}{r}\left[\left(N_T - \frac{dk_f}{\mu}\right)\frac{1}{\theta} + \frac{dk_g r}{\mu}\right]\right\}$ as shown in Panel D of Figure S8. Thus, If $C_T^{in} = \frac{d(1-r)}{r\theta}\left(N_T - \frac{dk_f}{\mu}\right)$, the system will have an infinite number of equilibrium points $E_4 = \left\{\left(A, \left(N_T - \frac{dk_f}{\mu}\right)\frac{1}{\theta}\right) : A > \frac{1}{r}\left[\left(N_T - \frac{dk_f}{\mu}\right)\frac{1}{\theta} + \frac{dk_g r}{\mu}\right]\right\}$

Thus an OSTP system may have 0, 1, or an infinite number of equilibrium points depending on the volume of fresh labile hydrocarbons input into the system, C_T^{in}. If $C_T^{in} > \frac{d(1-r)}{r\theta}\left(N_T - \frac{dk_f}{\mu}\right)$, the system will have no equilibrium point; if $C_T^{in} < \frac{d(1-r)}{r\theta}\left(N_T - \frac{dk_f}{\mu}\right)$, it will have one unique equilibrium point , $\left(\frac{\mu C_T^{in} + d^2 k_g(1-r)}{d(1-r)\mu}, \frac{rC_T^{in}}{d(1-r)}\right)$; and if $\frac{rC_T^{in}}{d(1-r)} = \left(N_T - \frac{dk_f}{\mu}\right)\frac{1}{\theta}$, it will have an infinite number of equilibrium points given by $\left\{\left(A, \left(N_T - \frac{dk_f}{\mu}\right)\frac{1}{\theta}\right) : A > \frac{1}{r}\left[\left(N_T - \frac{dk_f}{\mu}\right)\frac{1}{\theta} + \frac{dk_g r}{\mu}\right]\right\}$.

S2.2.1 Stability of equilibrium points in OSTP scenario:

To determine the local stability of the equilibria above, we consider the Jacobian matrix of System of equations (S1),

$$J(A,B) = \begin{pmatrix} 0 & \frac{(r-1)d}{r} \\ BG_A(A,B) & G(A,B) + BG_B(A,B) \end{pmatrix} \quad (S1.)$$

Where

$$G(A,B) = \begin{cases} \frac{\mu\left(A - \frac{B}{r}\right)}{k_g} - d \; if \; \frac{N_T - \theta B}{k_f} > \frac{A - \frac{B}{r}}{k_g} \\ \frac{\mu(N_T - \theta B)}{k_f} - d \; if \; \frac{N_T - \theta B}{k_f} < \frac{A - \frac{B}{r}}{k_g}, \end{cases}$$

$$G_A(A,B) = \begin{cases} \frac{\mu}{k_g} \; if \; \frac{N_T - \theta B}{k_f} > \frac{A - \frac{B}{r}}{k_g} \\ 0 \; if \; \frac{N_T - \theta B}{k_f} < \frac{A - \frac{B}{r}}{k_g} \end{cases}$$

and

$$G_B(A,B) = \begin{cases} \frac{-\mu}{k_g} \; if \; \frac{N_T - \theta B}{k_f} > \frac{A - \frac{B}{r}}{k_g} \\ \frac{-\theta}{k_f} \; if \; \frac{N_T - \theta B}{k_f} < \frac{A - \frac{B}{r}}{k_g} \end{cases}$$

Stability of E_1:

$$J(E_1) = \begin{pmatrix} 0 & \frac{(r-1)d}{r} \\ \frac{\mu r C_T^{in}}{k_g d(1-r)} & \frac{-C_T^{in}\mu}{d(1-r)k_g} \end{pmatrix} \quad (S2.)$$

Since $det\big(J(E_1)\big) = \frac{\mu C_T^{in}}{k_g}$ is greater than zero and $T_r\big(J(E_1)\big) = \frac{-C_T^{in}\mu}{d(1-r)k_g} < 0$, this implies that both eigenvalues of $J(E_1)$ have negative real parts. Hence E_1 is a locally stable equilibrium point. It is easy to see that E_1 is a stable spiral.

Stability of E_2:

$$J(E_2) = \begin{pmatrix} 0 & \frac{(r-1)d}{r} \\ 0 & \frac{-rC_T^{in}\mu\theta}{d(1-r)k_f} \end{pmatrix} \quad (S3.)$$

$\det\big(J(E_2)\big) = 0$ and $T_r\big(J(E_2)\big) = \frac{-rC_T^{in}\mu\theta}{d(1-r)k_f} < 0$.

Since the $T_r(J(E_2))$ is negative and $det(J(E_2))$ is zero, one eigenvalue is zero and the other is negative. Thus E_2 is a line of locally asymptotically stable equilibrium points. Hence both the

internal equilibrium point E_1 and the line of equilibrium points E_2 are locally asymptotically stable.

S2.2.2 End pit lake scenario ($C_T^{in} = 0$):

Steady states:

***A*-Nullclines:**

$$\dot{A} = 0 \implies B = 0$$

***B*-Nullclines:**

$$\dot{B} = 0 \implies B = 0 \; or \; G(A, B) = 0.$$

Panels C and D of Figure S7 show that, irrespective of the slope of the line $B = Ar - \frac{dk_g r}{\mu}$, the A-and B-nullclines have an infinite number of intersections, given by $E_5 = \{(A, 0): A \geq 0\}$. Thus for $C_T^{in} = 0$, system of equations (S1) has an infinite number of equilibrium points given by E_5.

Stability of E_5:

$$J(E_5) = \begin{pmatrix} 0 & \frac{(r-1)d}{r} \\ 0 & \frac{\mu A}{k_g} - d \end{pmatrix} \quad (4.)$$

$det\big(J(E_5)\big) = 0$ and $T_r\big(J(E_5)\big) = \frac{\mu A}{k_g} - d$. If $A < \frac{dk_g}{\mu}$, $T_r(J(E_5))$ will be less than zero and hence E_5 will be asymptotically stable. On the other hand, if $A \geq \frac{dk_g}{\mu}$, then $T_r(J(E_5))$ will be greater than 0 and thus E_5 will be a line of unstable equilibrium points.

S3. Qualitative challenge of model prediction

Figures S7 and S8 show eight theoretical in-situ scenarios presented as phase plane diagrams showing solutions for microbial biomass versus total carbon content (both unitless) under conditions of carbon or nitrogen limitation. The directional arrows account for time, nullclines define the vector fields, and nullcline intersections (fixed points) indicate regions where trajectories are horizontal or vertical; i.e., steady states. Panels S7A, S7B and S8A-S8D are relevant to the upper strata of OSTP where the input of labile hydrocarbon is continuous (i.e. $C_T^{in} > 0$) whereas Panels S7C and S7D represent an established EPL where labile carbon (as partially biodegraded diluent) enters the system with deposited MFT but is not replenished (i.e., $C_T^{in} = 0$) Furthermore, the availability of nitrogen (N_A) differs for each panel, as described below.

Let C_0^{in}, $C_1^{in}$and C_2^{in}denote sums of labile hydrocarbons with values $\left(N_T - \frac{dk_f}{\mu}\right)\frac{d(1-r)}{\theta r}$, $\left(\frac{C_T^{in}}{d(1-r)} + \frac{dK_g}{\mu}\right)$ and $\frac{1}{r}\left[\left(T - \frac{dk_f}{\mu}\right)\frac{1}{\theta} + \frac{dk_g r}{\mu}\right]$ respectively. Also, let B_0 and B_1 denote two different values of bacterial biomass. $B_0 = \left(N_T - \frac{dk_f}{\mu}\right)\frac{1}{\theta}$ and $B_1 = \frac{d(1-r)}{\theta r}$. Figures S7A and S8B show the predicted behaviour of OSTP in which the rate of input of hydrocarbons into the OSTP per unit time is $> C_0^{in}$. In this scenario, biomass moves towards B_0 (i.e., steady state). As biomass stabilizes, nitrogen becomes the limiting factor in microbial growth and thus bacteria consume only the amount of hydrocarbon permitted by N_A. This leads to a accumulation of hydrocarbon in the system due to the continuous influx of diluent and inability of bacteria to degrade all the carbon input. Such a scenario would require addition of N_A to the ponds to achieve additional diluent consumption, if that was the management goal. Conversely, restricting N_A in the pond should decrease CH_4 and CO_2 emissions although the potential for gas biogenesis

would persist for an indefinite period. Figures S7B and S8D illustrates the case of an OSTP where the rate of input of hydrocarbons into the OSTP per unit time is $< C_0^{in}$. In this case, biomass moves to a value of B_1 and total C_T^{in} moves to C_1^{in} . Because the total labile hydrocarbon deposited into the pond per unit time C_T^{in} is < C_0^{in}, carbon becomes the limiting factor for bacterial growth. Thus, biomass will increase to achieve a steady state at which carbon intake is maximized and all C_T is degraded as it enters the system. This scenario requires a continuous (but currently undiscovered) source of N_A in the tailings or the addition of exogenous N_A, i.e., as a management practice. The final possible scenario in OSTP is that depicted in Figures S8A and S8C. As with the other two cases above, we are equally looking at the OSTP as defined by the continuous input of carbon. Here the rate of input of hydrocarbons into the OSTP per unit time is C_0^{in}. At this influx value per unit time, nitrogen would be the limiting element for microbial growth. In this scenario, we have microbes growing to B_0, a point where they can maximize they nitrogen intake. Carbon in turn changes to a value that is greater than C_2^{in}.

The scenarios in Figures S7C and S7D simulate EPL conditions because $C_T^{in} = 0$. With extended time, C_T will approach a minimum (theoretically zero) as C_T is converted to CH_4 and dead biomass is likewise degraded after labile hydrocarbons are depleted. Figure S7C describes a scenario where the ratio of the nitrogen carrying capacity to carbon carrying capacity of the pond is < θr. Since there is no supply of exogenous carbon to the system, when the bacteria degrade all residual diluent, they ultimately have no carbon source other than dead biomass, which is converted to CH_4 and CO_2; eventually gas generation ceases in this closed system. Figure S7D predicts the situation where the ratio of the nitrogen carrying capacity to carbon carrying capacity of the pond is > θr but C_T still approaches zero because of the complete conversion of C_T and $\beta_T dB$ to gases, where β_T is the proportion of C_T contained in dead biomass that is

available for microbial recycling. Note that in the interim, biomass was greater than in Figure S7C because of the continuous presence of N_A.

REFERENCES:

AER, 2018. Statistical series ST 39 monthly report [WWW Document]. URL https://aer.ca/providing-information/data-and-reports/statistical-reports/st39 (accessed 4.24.19).

Burkus, Z., Wheler, J., Pletcher, S., 2014. GHG emissions from oil sands tailings ponds: Overview and modelling based on fermentable substrates. Alberta Environ. Sustain. Resour. Dev. https://doi.org/10.7939/R3F188

Codeco, C.T., Grover, J.P., 2001. Competition along a spatial gradient of resource supply: a microbial experimental model. Am. Nat. 157, 300–315.

Connolly, J.P., Coffin, R.B., Landeck, R.E., 1992. Modeling carbon utilization by bacteria in natural water systems. In: Hurst, C. J. (Ed.), Modelling the Metabolic and Physiologic Activities of Microorganisms. John Wiley, New York, 249–276.

Del Giorgio, P.A., Cole, J.J., 1998. Bacterial growth efficiency in natural aquatic systems. Annu. Rev. Ecol. Syst. 29, 503–541.

Foght, J.M., Gieg, L.M., Siddique, T., 2017. The microbiology of oil sands tailings: Past, present, future. FEMS Microbiol. Ecol. https://doi.org/10.1093/femsec/fix034

Roberts, D.J., 2002. Methods for assessing anaerobic biodegradation potential. In: Hurst, C.J., Crawford, R.L., Knudson, G.R., McInerney, M.J., Stetzenbach, L.D. (Eds.), Manual of Environmental Microbiology, second ed. ASM Press, USA, pp.1008–1017.

Mohamad Shahimin, M.F., Foght, J.M., Siddique, T., 2016. Preferential methanogenic biodegradation of short-chain n-alkanes by microbial communities from two different oil sands tailings ponds. Sci. Total Environ. 553, 250–257.

Mohamad Shahimin, M.F., Siddique, T., 2017a. Methanogenic biodegradation of paraffinic solvent hydrocarbons in two different oil sands tailings. Sci. Total Environ. 583, 115–122.

Mohamad Shahimin, M.F., Siddique, T., 2017b. Sequential biodegradation of complex naphtha hydrocarbons under methanogenic conditions in two different oil sands tailings. Environ. Pollut. 221, 398–406.

Siddique, T., Fedorak, P.M., Foght, J.M., 2006. Biodegradation of short-chain n-alkanes in oil sands tailings under methanogenic conditions. Environ. Sci. Technol. 40, 5459–5464.

Siddique, T., Fedorak, P.M., MacKinnon, M.D., Foght, J.M., 2007. Metabolism of BTEX and naphtha compounds to methane in oil sands tailings. Environ. Sci. Technol. 41, 2350–2356.

Siddique, T., Kuznetsov, P., Kuznetsova, A., Arkell, N., Young, R., Li, C., Guigard, S.,

887 Underwood, E., Foght, J.M., Raymond, J., Grunden, A.M., 2014. Microbially-accelerated
888 consolidation of oil sands tailings. Pathway I: changes in porewater chemistry. Front.
889 Microbiol. 5, 106. https://doi.org/10.3389/fmicb.2014.00106

890 Sterner, R.W., Elser, J.J., 2002. Ecological stoichiometry: the biology of elements from
891 molecules to the biosphere. Princeton University Press.

892 Symons, G.E., Buswell, A.M., 1933. The methane fermentation of carbohydrates1, 2. J. Am.
893 Chem. Soc. 55, 2028–2036.

894 Wang, H., Jiang, L., Weitz, J.S., 2009. Bacterivorous grazers facilitate organic matter
895 decomposition: a stoichiometric modeling approach. FEMS Microbiol. Ecol. 69, 170–179.

Table S1: Biodegradation and cumulative CH_4 production in cultures of Syncrude MFT incubated with Syncrude naphtha diluent.

Hydrocarbon (mg L^{-1})	**Incubation period (days)**									
	28	**77**	**142**	**216**	**249**	**271**	**365**	**475**	**605**	**730**
Toluene	46.0	38.2	0	0	0	0	0	0	0	0
Ethylbenzene	19.0	21.6	15.2	0	0	0	0	0	0	0
m-,*p*-Xylenes	35.0	46.2	35.0	36.9	28.7	10.1	7.7	0	0	0
o-Xylene	14.0	17.7	11.3	0	0	0	0	0	0	0
n-Hexane	5.0	2.5	2.7	1.2	0.7	0.4	0.4	0.3	0.3	0
n-Heptane	34.0	18.2	13.9	6.5	3.7	2.3	1.0	2.6	0	0
n-Octane	46.0	30.2	23.9	13.8	8.0	4.5	2.5	0	0	0
n-nonane	15.0	15.2	6.2	3.5	1.3	0	0	0	0	0
2-Methylhexane (2-MC_6)	10.0	6.8	6.0	6.9	6.4	5.3	4.7	5.7	2.7	1.6
3-Methylhexane (3-MC_6)	12.0	8.2	7.7	6.7	5.5	2.4	3.2	2.7	1.9	1.9
2-Methylheptane (2MC_7)	37.0	25.0	22.1	25.5	23.8	19.7	17.3	21.3	10.2	5.8
4-Methylheptane (4-MC_7)	14.0	9.6	8.4	8.4	4.4	3.5	4.4	4.5	3.4	0
Cumulative CH_4 production (µmol) *	16	114	416	774	955	893	1049	1039	1266	1248

* Cumulative methane is calculated by subtracting CH_4 produced by parallel endogenous control cultures (i.e., MFT not receiving additional naphtha) from CH_4 measured in test cultures (MFT receiving naphtha).

Table S2: Literature values for selected microbial parameters in system of equations (2)

Parameter *	Value Range	Unit	References
$\boldsymbol{\mu}$	1-4	d^{-1}	(Codeco and Grover, 2001; Connolly et al., 1992)
$\boldsymbol{r}$	0.31-0.75	– §	(Del Giorgio and Cole, 1998; Wang et al., 2009)
$\boldsymbol{\theta}$	$\frac{1}{9}-\frac{1}{4}$	– §	(Sterner and Elser, 2002)

* see Table 1, main text, for parameter definitions
–, unitless parameters

Table S3: Normalized mean square error (NMSE) values obtained by comparing the simulated biodegradation kinetics (generated using the system of equations (2) and parameter values in Table S4) to published experimental data for the 15 labile hydrocarbons (Table 2).

Hydrocarbon *	**NMSE**
n-Pentane	0.92
n-Hexane	0.99
n-Heptane	0.99
n-Octane	0.99
n-Nonane	0.98
n-Decane	0.99
Toluene	1.00
o-Xylene	1.00
m- plus *p*-Xylene	0.99
2-Methylpentane	1.00
3-Methylhexane	0.99
2-Methylheptane	0.95
4-Methylheptane	0.98
2-Methyloctane	0.85

*, NMSE values for 2-methylhexane, 2-methyloctane and 2-methylnonane cannot be calculated because the model-related parameter values for these hydrocarbons are not available from our laboratory experiments.

911 **Table S4:** Model parameters and their estimated values obtained from fitting data to the
912 solutions of the systems of equation (3).
913

Parameter *	Value	95% C.I.	Unit
$\boldsymbol{B(0)}$	0.0004	0.0001-0.0138	mmol C
$\boldsymbol{K_f}$	0.3	0.3	mmol
$\mathbf{N_T}$	327.6	327.1	mmol
$\boldsymbol{K_{g_{C_5}}}$	56.3	16.2-96.4	mmol
$\boldsymbol{K_{g_{C_6}}}$	430.3	366.1-494.5	mmol
$\boldsymbol{K_{g_{C_7}}}$	270.7	238.9-302.5	mmol
$\boldsymbol{K_{g_{C_8}}}$	90.1	69.3-110.9	mmol
$\boldsymbol{K_{g_{C_9}}}$	0.9	0.71-1	mmol
$\boldsymbol{K_{g_{C_{10}}}}$	12.0	10.2-13.9	mmol
$\boldsymbol{K_{g_{toluene}}}$	4.5	4.1-4.8	mmol
$\boldsymbol{K_{g_{m,p-Xylenes}}}$	85.1	76.9-93.2	mmol
$\boldsymbol{K_{g_{o-Xylenes}}}$	17.5	14.2-20.8	mmol
$\boldsymbol{K_{g_{2-MC_6}}}$ §	144.6	102.7-186.5	mmol
$\boldsymbol{K_{g_{3-MC_6}}}$	144.6	102.7-186.5	mmol
$\boldsymbol{K_{g_{2-MC_7}}}$	320.4	183.8-457.1	mmol
$\boldsymbol{K_{g_{4-MC_7}}}$	170.3	121.0-219.7	mmol
$\boldsymbol{K_{g_{2-MC_8}}}$	335.9	179.1-492.9	mmol
$\boldsymbol{K_{g_{3-MC_8}}}$ §	335.9	179.1-492.9	mmol
$\boldsymbol{K_{g_{2-MC_9}}}$ §	335.9	179.1-492.9	mmol
$\boldsymbol{K_{g_{2-MC_5}}}$	165.9	130.2-201.7	mmol
$\boldsymbol{C_5 - lag}$	200	200	days
$\mathbf{C_6 - lag}$	26	26	days
$\boldsymbol{C_7 - lag}$	60	40-80	days
$\mathbf{C_8 - lag}$	60	60	days
$\boldsymbol{C_9 - lag}$	70	70	days
$\boldsymbol{C_{10} - lag}$	5	5	days
$\boldsymbol{Toluene - lag}$	30	30	days
$\boldsymbol{m - and\ p - Xylenes - lag}$	70	70	days
$\boldsymbol{o - Xylenes - lag}$	60	60	days
$\mathbf{2 - MC_6 - lag}$ §	25	25	days
$\mathbf{3 - MC_6 - lag}$	25	25	days
$\mathbf{2 - MC_7 - lag}$	25	25	days
$\mathbf{4 - MC_7 - lag}$	25	25	days

$\mathbf{2-MC_8-lag}$	25	25	days
$\mathbf{3-MC_8-lag}$ §	25	25	days
$\mathbf{2-MC_9-lag}$ §	25	25	days
$\mathbf{2-MC_5-lag}$	23	23	days

* K_f represents the nitrogen-dependent half-saturation constant for microbial growth; N_T is the total nitrogen available in the system; $K_{g_{C_5}}$, $K_{g_{C_6}}$, $K_{g_{C_7}}$, $K_{g_{C_8}}$, $K_{g_{C_9}}$, $K_{g_{C_{10}}}$, $K_{g_{toluene}}$, $K_{g_{o-Xylenes}}$, $K_{g_{m,p-Xylenes}}$, $K_{g_{2-MC_6}}$, $K_{g_{3-MC_6}}$, $K_{g_{2-MC_7}}$, $K_{g_{4-MC_7}}$, $K_{g_{2-MC_8}}$, $K_{g_{3-MC_8}}$, $K_{g_{2-MC_8}}$, $K_{g_{2-MC_9}}$, $K_{g_{2-MC_5}}$ respectively represent the half-saturation constants for microbial growth on C_5-, C_6-, C_7-, C_8-, C_9-, C_{10}- *n*-alkanes, toluene, o-xylene, m- plus p-xylene, 2-methylhexane-, 3-methylhexane-, 2-methylheptane-, 4-methylheptane-, 2-methyloctane-, 3-methyloctane-, 2-methylnonane- and , 2-methylpentane-. *Z*-lag denotes a lag period of *Z*, where Z is one of C_5, C_6, C_7, C_8, C_9, C_{10}, toluene, *o*-xylene, *m*- plus *p*-xylene, 2-methylhexane-, 3-methylhexane, 2-methylheptane, 4-methylheptane, 2-methyloctane 3-methyloctane, 2-methylnonane or 2-methylpentane.

§ The values of model parameters K_g and lag for 2-MC_6, 3-MC_8 and 2-MC_9 were not available from empirical studies and are assumed to be the same as those for 3-MC_6, 2-MC_8 and 2-MC_8, respectively, based on their similar molecular weights.

930 **Table S5**: Estimated zero-and first-order model parameter values for labile diluent hydrocarbons
931 not reported by Siddique et al. (2008).
932

Hydrocarbon	Lag phase (d)	Zero-order parameter (mmole d^{-1})	First-order parameter (d^{-1})
n-Pentane	294	0.0008576	0.01117
n-Nonane	77	2.664e-05	0.01276
2-Methylpentane	600	0.0002281	0.003501
3-Methylhexane	455	0.0001816	0.003849
2-Methylheptane	845	0.00023	0.005258
4-Methylheptane	665	0.0001936	0.005663
2-Methyloctane	665	0.0001772	0.0006584

933

Table S6. Calculation of mass balance of diluent entering OSTP in 2016 and 2017. These values are used in Table S8 calculations.

	Syncrude MLSB		CNRL Horizon		CNUL MRM	
	2016	2017	2016	2017	2016	2017
Reported mass of diluent lost to fresh tailings before deposition in OSTP (t) [a]	57,336	43,032	24,722	35,295	28,558	32,494
Estimated mass of diluent lost from OSTP by volatilization (t) [b]	(-17,201)	(-12,910)	(-7,416)	(-10,589)	(-11,423)	(-12,998)
Calculated net mass of diluent remaining in OSTP (t)	40,135	30,122	17,305	24,706	17,135	19,496

a, Data retrieved from Alberta Energy Regulator ST 39 report (AER, 2018) and calculated using the reported volume of diluent loss (m^3) and multiplying by the respective densities of diluents (Syncrude naphtha, 0.76 t m^{-3}; CNRL naphtha, 0.73 t m^{-3}; and CNUL paraffinic solvent, 0.65 t m^{-3} (Burkus et al., 2014).

b, A factor of 0.7 (i.e., 30% volatilization) was used for Syncrude and CNRL naphtha diluents and a factor of 0.6 (i.e., 40% volatilization) was used for CNUL paraffinic diluent to calculate the mass of diluent volatilized from OSTP per Burkus et al. (2014) .

945 **Table S7.** Concentrations of 18 labile hydrocarbons in diluents and calculated masses of labile
946 diluent hydrocarbons present in tailings entering OSTP in 2016 and 2017. Values are used in
947 Table S8 calculations.

	Syncrude MSLB			CNRL Horizon			CNUL MRM		
Labile hydrocarbon	% of naphtha diluent [a]	mass in OSTP (t) 2016 [b]	mass in OSTP (t) 2017 [b]	% of naphtha diluent [a]	mass in OSTP (t) 2016 [b]	mass in OSTP (t) 2017 [b]	% of paraffinic diluent [a]	mass in OSTP (t) 2016 [b]	mass in OSTP (t) 2017 [b]
Toluene	6.11	2452	1840	0	0	0	0	0	0
m-, *p*-Xylene	4.64	1862	1398	0	0	0	0	0	0
o-Xylene	1.78	714	536	0	0	0	0	0	0
n-C_5	0	0	0	0	0	0	24.00	4112	4679
n-C_6	0.60	241	181	3.85	666	951	11.26	1929	2195
n-C_7	4.50	1806	1356	9.35	1618	2310	0	0	0
n-C_8	6.05	2428	1822	4.65	805	1149	0	0	0
n-C_9	1.99	799	599	1.70	294	420	0	0	0
n-C_{10}	0.31	126	94	1.65	286	408	0	0	0
2-MC_5	0	0	0	1.25	216	309	23.50	4027	4582
2-MC_6	1.30	522	392	5.30	917	1309	0	0	0
3-MC_6	1.51	607	456	5.05	874	1248	0	0	0
2-MC_7	4.92	1976	1483	3.85	666	951	0	0	0
4-MC_7	1.86	747	561	1.25	216	309	0	0	0
2-MC_8	1.16	465	349	1.00	173	247	0	0	0
3-MC_8	1.55	623	467	0.55	95	136	0	0	0
2-MC_9	0.31	124	93	2.90	502	717	0	0	0
% of diluent considered labile	39			42			59		
Total mass of labile hydrocarbon entering OSTP (t)		15492	11627		7329	10463		10068	11456

948
949 [a] The concentrations of individual hydrocarbons in Syncrude and CNRL naphtha diluents were
950 calculated using PONAU analysis reported by (Siddique et al., 2007) and (Mohamad Shahimin,
951 and Siddique, 2017b), respectively, and the concentrations of individual hydrocarbons in CNUL
952 paraffinic diluent were calculated using the PONAU analysis reported by (Mohamad Shahimin
953 and Siddique, 2017a).
954 [b] The data were retrieved from Alberta Energy Regulator report ST 39 (AER, 2018)
955

Table S8: Contribution of individual labile diluent hydrocarbons to the maximum theoretical cumulative yield of CH_4 from OSTPs in 2016 and 2017, based on masses calculated in Tables S5 and S6). Methane yield was calculated using equation (4) in main text, per Symons and Buswell (1933) as implemented by Roberts (2002).

	Calculated theoretical methane production (moles x 10^6)					
Labile hydrocarbon	**Syncrude MLSB**	**CNRL Horizon**	**CNUL MRM**	**Syncrude MLSB**	**CNRL Horizon**	**CNUL MRM**
	2016			**2017**		
Toluene	120	0	0	90	0	0
m-, *p*-Xylene	92	0	0	69	0	0
o-Xylene	35	0	0	27	0	0
n-C_5	0	0	228		0	259
n-C_6	13	37	106	10	52	121
n-C_7	99	89	0	74	127	0
n-C_8	133	44	0	100	63	0
n-C_9	44	16	0	33	23	0
n-C_{10}	7	16	0	5	22	0
2-MC_5	0	12	222	0	17	253
2-MC_6	29	50	0	21	72	0
3-MC_6	33	48	0	25	69	0
2-MC_7	108	36	0	81	52	0
4-MC_7	41	12	0	31	17	0
2-MC_8	25	9	0	19	14	0
3-MC_8	34	5	0	25	7	0
2-MC_9	7	27	0	5	39	0
Total theoretical methane (moles x 10^6) [a]	820	401	556	615	574	633
Microbial hydrocarbon conversion to methane (moles x 10^6) [b]	656	321	445	492	459	506
Total methane emissions from ponds (moles x 10^6) [C]	1191	336	2634	991	599	1051
Contribution of diluent hydrocarbons to total methane emissions from ponds (%)	55	95	17	50	77	48

[a] The masses of individual hydrocarbons from Table S6 were converted into moles using the respective molecular weights and then Symons and Buswell equation (per Roberts, 2002) was used to calculate theoretical maximum methane production from individual hydrocarbons.

[b] A factor of 0.8 determined during our hydrocarbon biodegradation studies (Siddique et al., 2007, 2006) was used to calculate the efficiency of microbial conversion of hydrocarbons to methane; i.e., r_i

[C] CH_4 emission data (unpublished data, Government of Alberta) were converted into moles for comparison. The Government of Alberta data includes CH_4 emissions from all units. We considered only those units that had been receiving froth treatment tailings (solvent containing stream) for the most recent two or three years. Therefore, for comparison, the bubbling zone of Syncrude MLSB, the entire CNRL Horizon pond and Cells 1-3 of CNUL receiving diluent containing streams were used for field emissions data.

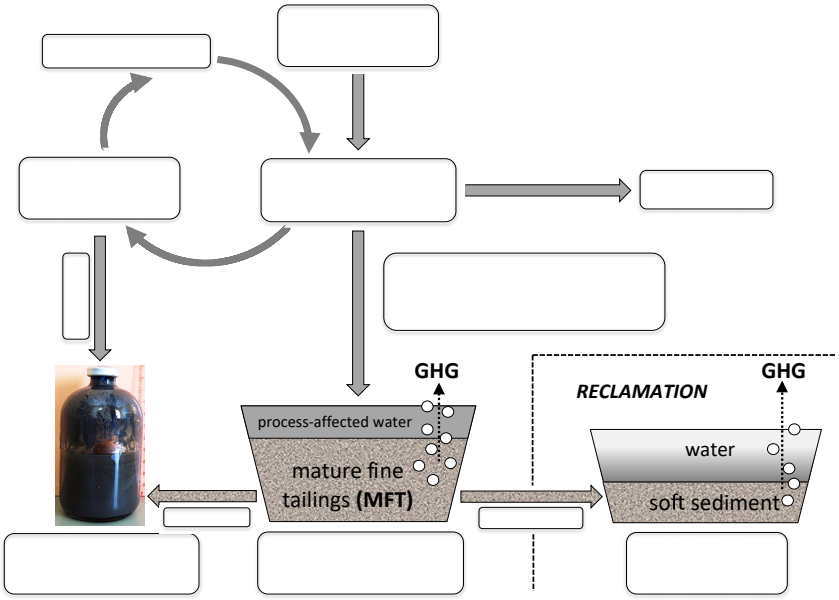

Figure S1. Simplified schematic of aqueous bitumen extraction from surface-mined oil sands, with subsequent retention of tailings in oil sands tailings ponds (OSTP) and reclamation in end pit lakes (EPL) (reviewed Foght et al., 2017). Biogenic gases in tailings (1) may escape to the atmosphere from shallow sediments via ebullition as greenhouse gas (GHG) emissions during retention or from deeper sediments when physically disturbed (e.g., by mechanical transfer), or (2) may be trapped as temporary or permanent gas voids (Guo, 2009) in dense sediments as latent GHG emissions, or (3) may be immobilized and transformed via geochemical interactions with clay minerals and pore water (Siddique et al., 2014).

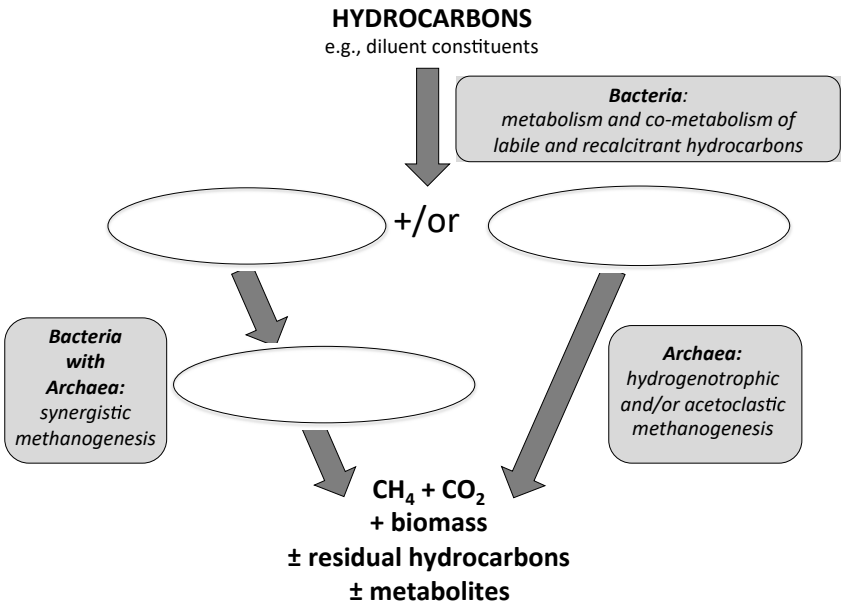

Figure S2. Simplified biochemical flowchart for methanogenic biodegradation of hydrocarbons. Metabolic processes carried out by bacteria or archaea alone or by synergistic consortia are indicated in italics. If sulfate is present in sufficient concentrations (e.g., via addition of gypsum [$CaSO_4 \cdot 2H_2O$] in some oil sands tailing processes; Foght et al., 2017), anaerobic biodegradation may still proceed but will be skewed toward accumulation of metabolites plus CO_2 and biomass, with minimal CH_4 production. The ultimate end products include GHG, biomass, non-degradable hydrocarbons and dead-end metabolites, e.g., from partial oxidation of recalcitrant hydrocarbons.

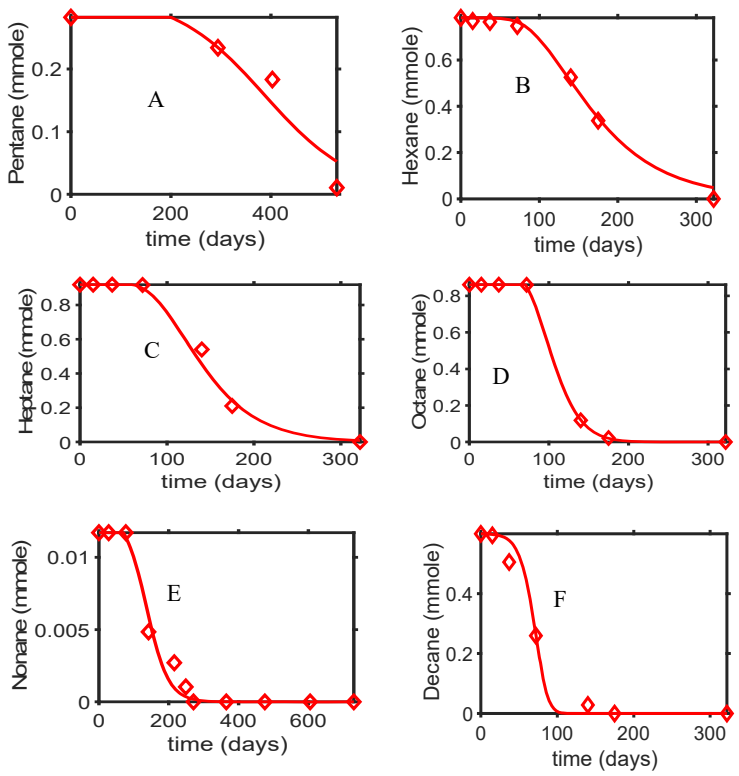

Figure S3. System of equations (2) fit to measured *n*-alkane biodegradation values for laboratory cultures. Symbols denote measured values and lines represent best fits to the data. Panels A, B, C, D, E and F show results for *n*-pentane, *n*-hexane, *n*-heptane, *n*-octane, *n*-nonane, and *n*-decane, respectively.

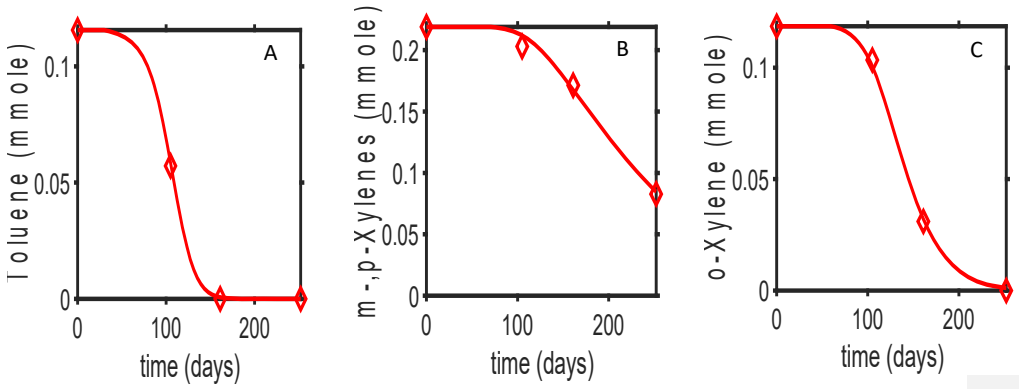

Figure S4. System (2) fit to measured biodegradable monoaromatic compound data for laboratory cultures. Diamond symbols denote measured values and solid lines represent fitted values. Panels A, B and C respectively show results for toluene, *m*- plus *p*-xylene, and *o*-xylene.

1007

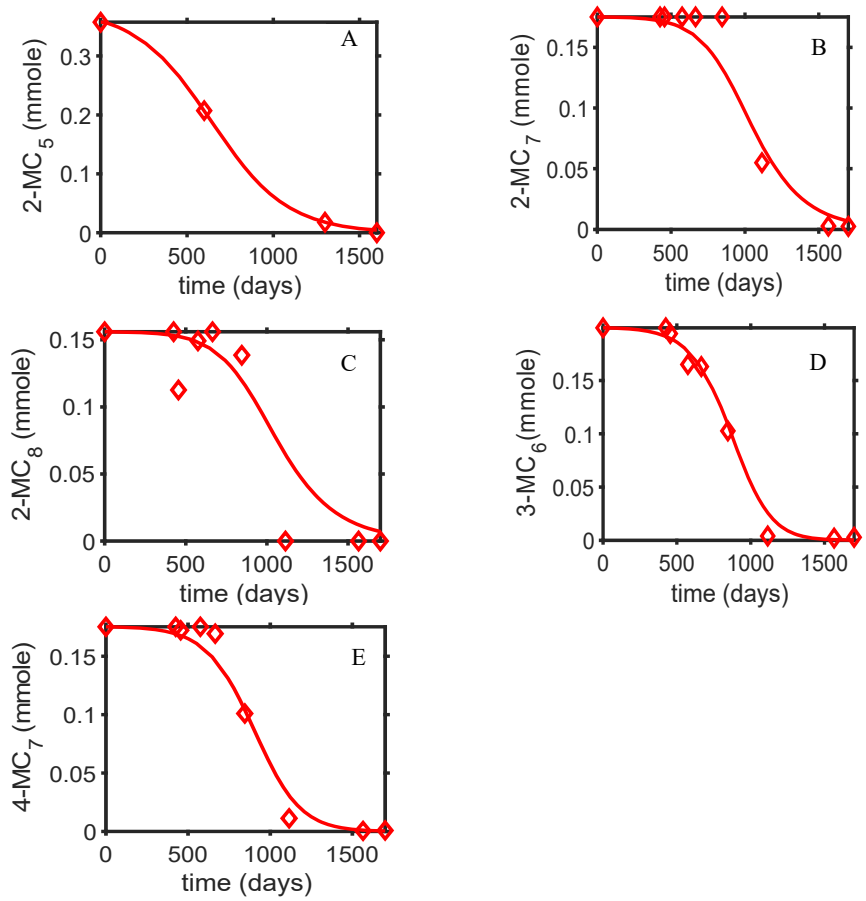

1008
1009
1010
1011

1012 **Figure S5.** System (2) fit to *iso*-alkane biodegradation measurements for laboratory cultures.
1013 Solid lines represent fitted values and diamonds denote measured values. Panels A, B, C, D and
1014 E show results for 2-methylheptane, 2-methyloctane, 2-methylpentane, 3-methylhexane and 4-
1015 methylheptane, respectively.

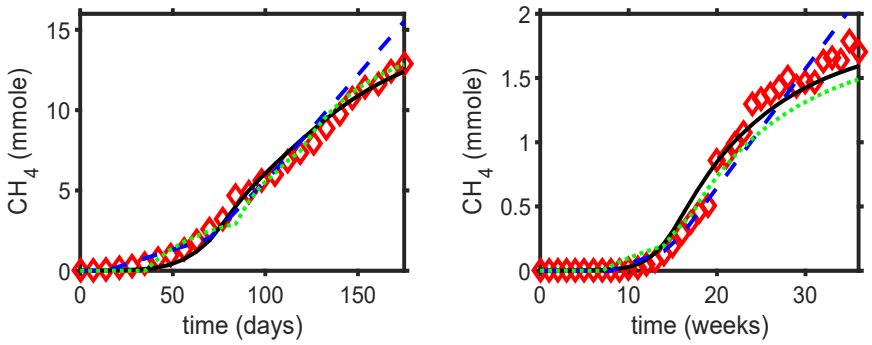

Figure S6: Comparison of stoichiometric model predictions of methane production from laboratory cultures of Syncrude MFT incubated with mixtures of either *n*-alkane (C_6, C_7, C_8 and C_{10}) or monoaromatic (toluene, *o*-, *m*- and *p*-xylenes) components of naphtha diluent (left and right panels, respectively). Measured methane values, from laboratory experiments independent of those used to develop the model, are shown by diamond symbols. Solid black lines represent the stoichiometric model prediction; broken blue lines and dotted green lines respectively represent predictions made by using the previous zero-order and first-order models (Siddique et al., 2008).

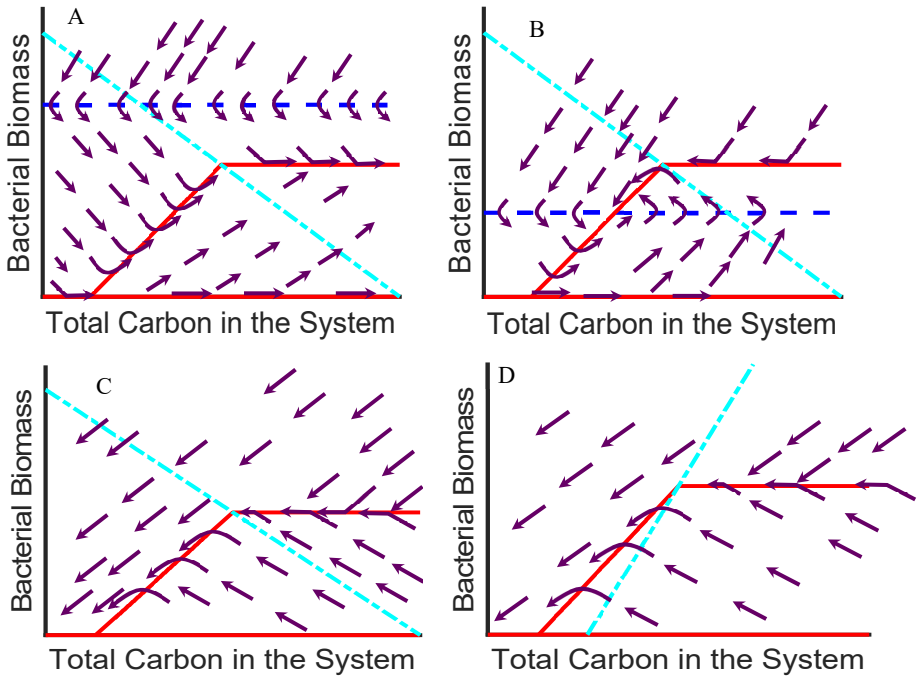

Figure S7: Phase plane analysis of solution states for microbial biomass and total carbon content in OSTP (Panels A and B, where $C^{in} > 0$) or EPL (Panels C and D, where $C_T^{in} = 0$) under different assumed initial conditions of C_T^{in} and ratio of the nitrogen carrying capacity to carbon carrying capacity ($k_f : k_g$). In Panel A: $C_T^{in} > \left(N_T - \frac{dk_f}{\mu}\right)\frac{d(1-r)}{\theta r}$ and $k_f : k_g < \theta r$. In Panel B, $C_T^{in} < \left(N_T - \frac{dk_f}{\mu}\right)\frac{d(1-r)}{\theta r}$ and $k_f : k_g < \theta r$. In Panel C: $k_f : k_g < \theta r$. In Panel D: $k_f : k_g > \theta r$. Solid red lines are nullclines for total biomass, broken blue lines are nullclines for total carbon content and broken light blue lines indicate where $B = \left(N_T - \frac{\left(C_T + \frac{B}{r}\right)k_f}{k_g}\right)\left(\frac{k_g r}{\theta k_g r - k_f}\right)$, to the left of which nitrogen is limiting and to the right of which carbon is limiting. The slope of this line is determined by the ratio: $k_f : k_g$. Purple directional arrows account for time.

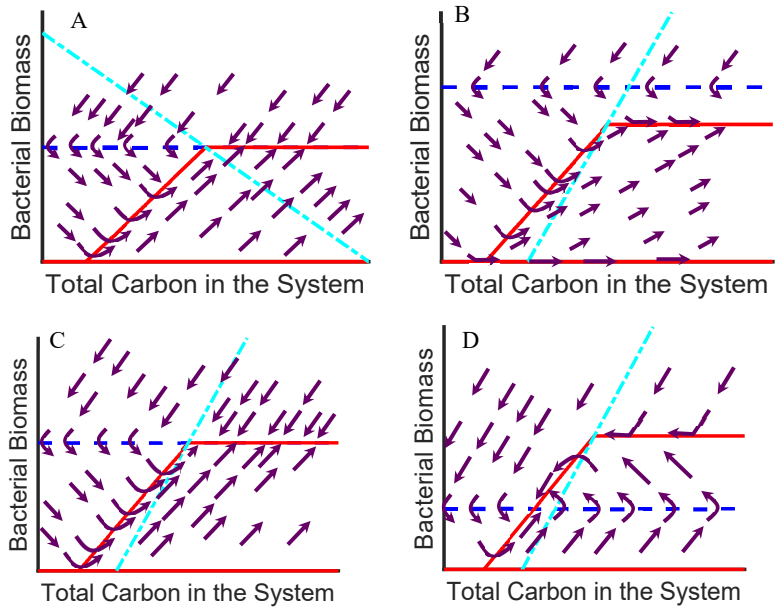

Figure S8: Phase plane analysis of solution states for microbial biomass and total carbon content in OSTP (where $C^{in} > 0$) under different assumed initial conditions of C_T^{in} and ratio of the nitrogen carrying capacity to carbon carrying capacity ($k_f : k_g$). In Panel A: $C_T^{in} = \left(N_T - \frac{dk_f}{\mu}\right)\frac{d(1-r)}{\theta r}$ and $k_f : k_g < \theta r$. In Panel B, $C_T^{in} > \left(N_T - \frac{dk_f}{\mu}\right)\frac{d(1-r)}{\theta r}$ and $k_f : k_g > \theta r$. In Panel C: $C_T^{in} = \left(N_T - \frac{dk_f}{\mu}\right)\frac{d(1-r)}{\theta r}$ and $k_f : k_g > \theta r$. In Panel D: $C_T^{in} < \left(N_T - \frac{dk_f}{\mu}\right)\frac{d(1-r)}{\theta r}$ and $k_f : k_g > \theta r$. Solid red lines are nullclines for total biomass, broken blue lines are nullclines for total carbon content and broken light blue lines indicate where the line $B = \left(N_T - \frac{\left(C_T + \frac{B}{r}\right)k_f}{k_g}\right)\left(\frac{k_g r}{\theta k_g r - k_f}\right)$ to the left of which nitrogen is limiting and to the right of which carbon is limiting. The slope of this line is determined by the ratio: $k_f : k_g$. Purple directional arrows account for time.